

Sensitivity of Wind Turbine Array Downstream Effects to the Parameterization Used in WRF

T. J. SHEPHERD

Department of Earth and Atmospheric Sciences, Cornell University, Ithaca, New York

R. J. BARTHELMIE

Sibley School of Mechanical and Aerospace Engineering, Cornell University, Ithaca, New York

S. C. PRYOR

Department of Earth and Atmospheric Sciences, Cornell University, Ithaca, New York

(Manuscript received 3 June 2019, in final form 5 December 2019)

ABSTRACT

The Weather Research and Forecasting (WRF) Model has been extensively used for wind energy applications, and current releases include a scheme that can be applied to examine the effects of wind turbine arrays on the atmospheric flow and electricity generation from wind turbines. Herein we present a high-resolution simulation using two different wind farm parameterizations: 1) the “Fitch” parameterization that is included in WRF releases and 2) the recently developed Explicit Wake Parameterization (EWP) scheme. We compare the schemes using a single yearlong simulation for a domain centered on the highest density of current turbine deployments in the contiguous United States (Iowa). Pairwise analyses are applied to diagnose the downstream wake effects and impact of wind turbine arrays on near-surface climate conditions. On average, use of the EWP scheme results in small-magnitude wake effects within wind farm arrays and faster recovery of full WT array wakes. This in turn leads to smaller impacts on near-surface climate variables and reduced array–array interactions, which at a systemwide scale lead to summertime capacity factors (i.e., the electrical power produced relative to nameplate installed capacity) that are 2%–3% higher than those from the more commonly applied Fitch parameterization. It is currently not possible to make recommendations with regard to which wind farm parameterization exhibits higher fidelity or to draw inferences with regard to whether the relative performance may vary with prevailing climate conditions and/or wind turbine deployment configuration. However, the sensitivities documented herein to the wind farm parameterization are of sufficient magnitude to potentially influence wind turbine array siting decisions. Thus, our research findings imply high value in undertaking combined long-term high-fidelity observational studies in support of model validation and verification.

1. Introduction

Wind turbines (WT) generate electricity by extracting kinetic energy from the atmospheric flow and converting that mechanical energy into electric energy. Behind each WT and behind clusters of WT (i.e., downstream of WT arrays) the flow exhibits a “wake” characterized by lower mean velocity and increased turbulence intensity (Barthelmie et al. 2013; Wu and Porté-Agel 2013). The velocity deficit downstream of WT [i.e., the reduction of

wind speed relative to what would be present in the absence of WT (the freestream)] is of greatest magnitude directly behind WT. As the downstream distance increases, the wake expands vertically and horizontally, higher momentum air is drawn into the wake, and at sufficient distances downstream the wind profile recovers to be equal to that in undisturbed conditions (Barthelmie and Pryor 2013).

Utility-scale WT deployments currently supply over 6% of U.S. electricity demand (National Renewable Energy Laboratory 2015). In 2008, the National Renewable Energy Laboratory outlined a feasibility study of 20% wind power supply delivered to the U.S. electrical grid

Corresponding author: S. C. Pryor, sp2279@cornell.edu; Tristan Shepherd, tristan.shepherd@cornell.edu

by 2030 (National Renewable Energy Laboratory 2008). An updated feasibility study (*Wind Vision*) indicated 35% penetration of the U.S. national electricity supply was possible by 2050 (National Renewable Energy Laboratory 2015). These projections indicate installed wind energy capacity would need to grow from the current installed capacity of 84 GW (2017) to approximately 113 GW by 2020, 224 GW by 2030, and 404 GW by 2050 (National Renewable Energy Laboratory 2015). The research in this paper is designed to quantify the impact of large WT arrays on downstream conditions and thus to lay ground work for research to examine whether expansion of WT deployments proposed in the national feasibility studies may result in substantial WT array–array interactions where downstream WT arrays experience lower resource magnitudes due to disruption of the flow by upstream WT, and/or inadvertent climate modification at the local scale due to the increase in atmospheric turbulence.

A number of previous studies have 1) examined inadvertent climate impacts from WT arrays, 2) sought to derive limits on systemwide extraction of kinetic energy, or 3) explored ways to optimize wind farm layouts to minimize array–array interactions. Initial numerical work in this field employed a range of tools of varying complexity (including roughness blocks) to represent the momentum drag imposed by WT and found significant and far reaching climate impacts (e.g., Baidya Roy 2011; Baidya Roy et al. 2004; Barrie and Kirk-Davidoff 2010; Fiedler and Bukovsky 2011; Keith et al. 2004; Wang and Prinn 2010). More recent work that has used limited-area regional models [e.g., the Weather Research and Forecasting (WRF) Model; Skamarock et al. 2008] has employed more realistic and explicit wind farm parameterizations and has generally found more modest impacts on the atmosphere (e.g., Cervarich et al. 2013; Fitch et al. 2013, 2012; Pryor et al. 2018a,c; Vautard et al. 2014; Wang et al. 2019; Xia et al. 2017) except when unrealistically high WT densities over very large areas are postulated to examine theoretical limits on kinetic energy extraction (Miller et al. 2015). The most commonly used explicit wind farm parameterization was developed by A. Fitch (Fitch et al. 2012) (see detailed description in section 2). Wind turbine wakes from this parameterization have been shown to be sensitive to the model configuration employed (especially the vertical resolution) (Fitch et al. 2012; Lee and Lundquist 2017) and to exhibit a positive bias in wake intensity (Lee and Lundquist 2017). A previous analysis using this wind farm parameterization found changes in near-surface temperatures near WT arrays arose primarily via changes in the sensible heat flux and that the addition of turbulent kinetic energy over the wind farm

also contributed to near-surface warming, while the momentum sink component led to cooling downstream (Xia et al. 2019).

Observational studies of far-field wind turbine wakes have also been conducted using in situ and ground-based remote sensing measurement techniques (e.g., Baidya Roy and Traiteur 2010; Rajewski et al. 2013; Smith et al. 2013) and data from satellite-based radiometers (e.g., Harris et al. 2014; Zhou et al. 2012). The latter studies are constrained to include only cloud-free conditions and have tended to show larger impacts on near-surface temperatures close to wind turbine arrays.

Here, we extend the literature by conducting and analyzing a high-resolution WRF simulation using two different wind farm parameterizations: 1) the Fitch parameterization (Fitch et al. 2012) that is included in WRF releases and 2) the recently developed Explicit Wake Parameterization (EWP) scheme (Volker et al. 2015). Our objective is to quantify differences in wind farm wakes generated in the two schemes (Fig. 1) and the implications for downstream climate impacts and the systemwide efficiency of electrical power production. The model domain over which these WT parameterizations are applied is shown in Fig. 2 (note that there are four domains in this simulation: domain 1 is the parent nest and domain 2 contains no WT; domains 3 and 4 operate the Fitch and EWP schemes, respectively).

2. Materials and methods

a. Wind farm parameterization schemes

The wind farm parameterizations employed herein were both developed for inclusion within the WRF Model (Skamarock et al. 2008). This limited-area model has been widely used and evaluated within both the climate science (e.g., Gao et al. 2012; Mearns et al. 2012; Sun et al. 2016; Wang and Kotamarthi 2014) and wind energy communities (e.g., Draxl et al. 2014; Hahmann et al. 2015; Pryor and Hahmann 2019; Pryor et al. 2018a,b). The wind farm parameterizations used in this limited-area modeling context are not designed to represent the wakes from individual WT but rather to describe the cumulative drag imposed on the mean flow by all WT within a model grid cell. In both wind farm schemes presented herein (see schematic in Fig. 1), the drag force imposed by the WT is determined from the thrust coefficient, which is a function of WT type and the wind speed. This force is only applied to model levels containing the turbine blades (i.e., over the rotor-swept area) and leads to a velocity deficit profile and thus shear within the wind profile. A WT specific power curve is applied to generate an estimate of gross

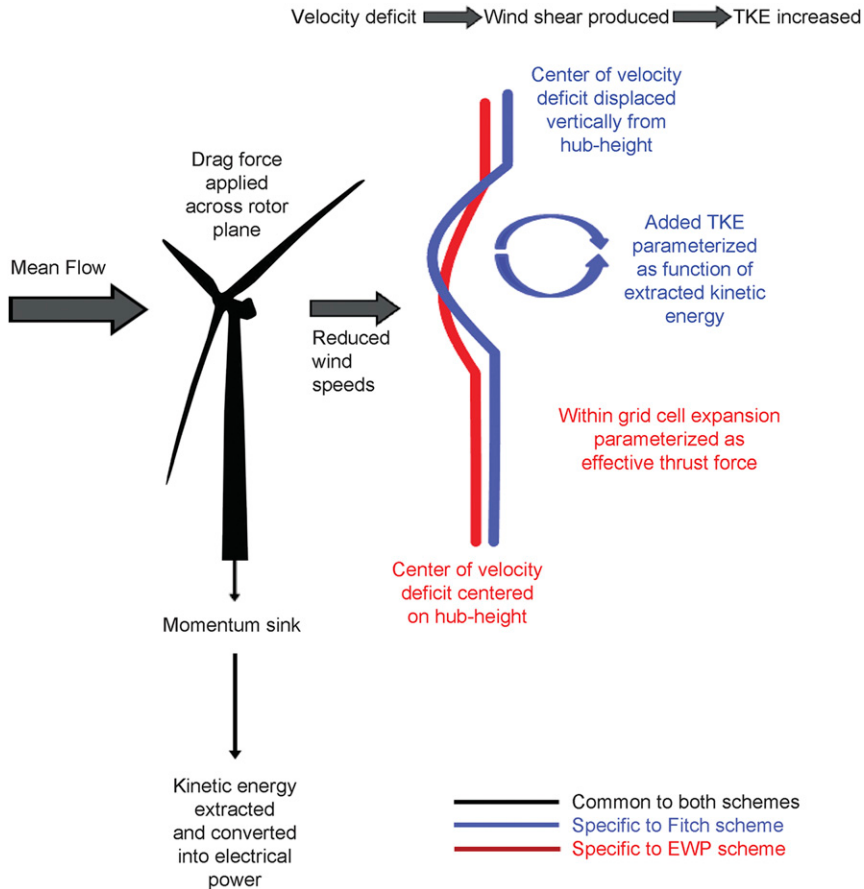


FIG. 1. Simple schematic showing the key features and major differences of the Fitch and EWP schemes.

electrical power production as a function of incident wind speed (Fig. 3b).

The primary difference between EWP and Fitch wind farm parameterizations is that while the Fitch scheme applies additional turbulent kinetic energy (TKE) to all model grid cells that intersect the turbine rotor, the EWP scheme parameterizes the unresolved wake expansion within the grid cell due to enhanced turbulence. Additional TKE in both schemes is introduced from the modified wind speed profile due to the WT wake(s). These differences can be further illustrated using the following simplified budget for TKE:

$$\frac{\partial \bar{e}}{\partial t} = \bar{P}_s + \bar{P}_b + \bar{P}_t - \bar{T} - \epsilon, \quad (1)$$

where $\partial e/\partial t$ is the rate of change of TKE in a given grid cell, \bar{T} is TKE transport (advection by the mean flow, turbulent transport, and the divergence of the pressure correlation), \bar{P}_s is production from the vertical shear in the horizontal velocity, \bar{P}_b is production or destruction

related to buoyancy forces, \bar{P}_t is TKE induced by the turbine rotor, and ϵ is the dissipation.

In the Fitch parameterization (Fitch et al. 2012; Fitch 2016), TKE induced by the turbine rotor is described as the fraction of kinetic energy extracted by the WT that is not converted into electrical power [shown as Eq. (2) below, from Fitch et al. [2012, their Eq. (12)]]:

$$\frac{\partial \text{TKE}_{ijk}}{\partial t} = \frac{0.5N_i^{ij}C_{\text{TKE}}(|V|_{ijk})|V|_{ijk}^3A_{ijk}}{z_{k+1} - z_k}, \quad (2)$$

where $\partial \text{TKE}/\partial t$ is the rate of change of TKE in a grid cell i, j at a vertical level k resulting from the action of WT, N_i is the number of wind turbines per square meter, C_{TKE} is the fraction of energy converted into TKE (described by the difference in the wind turbine thrust and power coefficients), z_k is height at model level k , V is the horizontal wind speed (from the components u and v), and A_{ijk} is the cross-sectional rotor area [$A = (\pi/4)D^2$, where D is the diameter of the turbine blades].

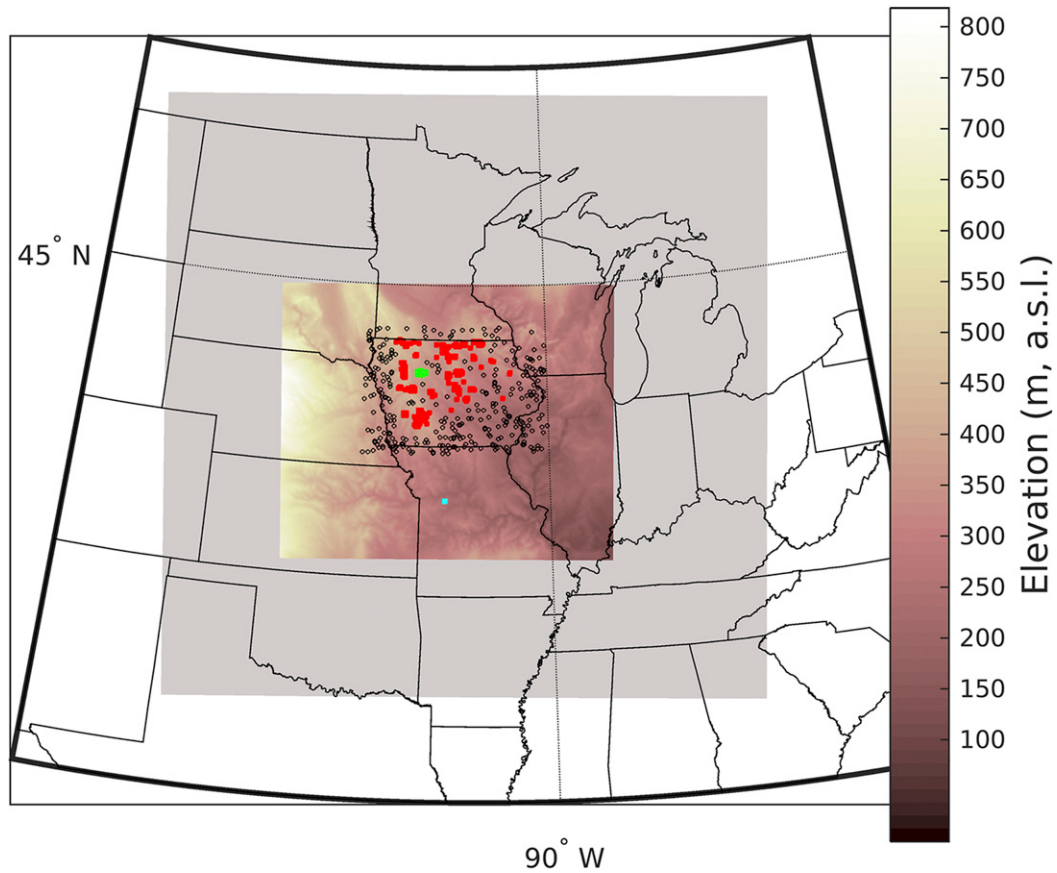


FIG. 2. Model domain configuration used for this simulation. The outer domain (domain 1; gray box) has a resolution of 12 km, and the three identical inner-nest domains [i.e., domain 2 (contains no WT), domain 3 (operates the Fitch wind farm parameterization), and domain 4 (operates the EWP wind farm parameterization)], defined by the elevation overlay, are 4 km. The 4-km grid cells in Iowa that contain one or more WT at the end of 2014 are shown in red. The wind farm cluster denoted by the green markers is the Pomeroy and Pocahontas Prairie wind farms. The cyan marker is the grid cell from Missouri that is used to characterize the background flow climate. The black markers are the 256 randomly selected background grid cells used in analyses of the regional climate impact.

In EWP (Volker et al. 2015), the WT are not treated as an active source of TKE. Instead any added TKE resulting from the action of the WT derives solely from shear production (i.e., is the result of the vertical shear). The increase in gridcell average turbulence resulting from WT is instead treated by inclusion in the scheme of within gridcell expansion of the wake in the vertical direction using a subgrid turbulence diffusion equation, which in turn determines a gridcell-averaged force added back to the model flow equation. The turbulence diffusion equation is represented as

$$\bar{u}_0 \frac{\partial}{\partial x} (\bar{u}_0 - \hat{u}) = K \frac{\partial^2}{\partial z^2} (\bar{u}_0 - \hat{u}) + K \frac{\partial^2}{\partial y^2} (\bar{u}_0 - \hat{u}), \quad (3)$$

where $\bar{u}_0 - \hat{u}$ describes the expansion of the velocity deficit behind the turbine, $\bar{u}_0 = |\bar{u}(h, t)|$ is the advection velocity at hub height, $\hat{u}(x)$ is the unresolved velocity in

the streamwise direction x in the wake of the turbine, and K is a turbulence diffusion coefficient. Crucial to the effective thrust force is the definition of the effective length scale σ that determines the wake expansion [Volker et al. 2015; their Eq. (7)]:

$$\sigma^2 = \frac{2K}{\bar{u}_0} x + \sigma_0^2. \quad (4)$$

The initial length scale σ_0 is not known a priori but scales with the wind turbine rotor length. Analyses of varying the length scale over the range from $\sigma_0 = D/2$ to $\sigma_0 = D$ led to a best fit to downstream wind speeds for $\sigma_0 = 0.85D$ based on a wind farm comprising Vestas V80 2-MW WT in the North Sea (Horns Rev I; Volker et al. 2015). We acknowledge the appropriate value for σ_0 may differ from that of Volker et al. (2015) but note that 1) relatively little sensitivity was observed for

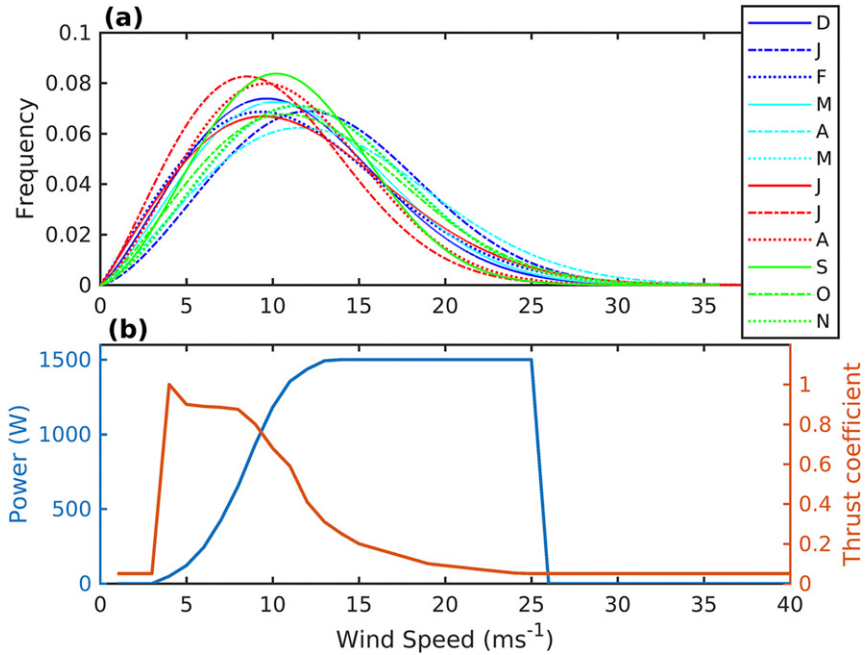


FIG. 3. (a) Monthly Weibull distribution fits to 10-min wind speeds for the third model layer ($\sim 100 \text{ m AGL}$) from the inner-domain subregion over Iowa from d02 that is operated without WT. The parameters of the Weibull distributions were derived from the 10-min output using maximum likelihood methods (Pryor et al. 2004). (b) Power and thrust curve for a GE 1.5-MW WT that dominates WT deployed in the Pomeroy wind farm cluster (see details in Table 1).

$\sigma_0 = 0.75D - 0.95D$ [i.e., the wind speed deficit relative to the freestream varied by $< 1\%$ for downstream distances of up to 5 km; see Fig. 4 of Volker et al. (2015)] and that 2) in Iowa more than 50% of the WT used in the present study have a hub height and rotor diameter that is close to the Horns Rev I wind turbines, which have a hub height of 70 m and rotor diameter of 80 m.

A further key difference between the two parameterizations pertains to the way in which the drag is applied in the vertical coordinate. In the Fitch scheme the application in the z coordinate means that the wake center is “lofted” from the WT hub height (HH). Another minor difference in the two schemes pertains to the allocation of geolocated WT to individual WRF grid cells. In work presented herein, the EWP scheme has been modified to use the gridcell allocation as applied in Fitch.

Our a priori expectation is that wind farm wakes will exhibit different near-field intensity and downstream propagation due to the fundamental differences in the two schemes described above. We further hypothesize that use of the Fitch scheme would induce stronger near-array effects than EWP because of the inclusion in EWP of the within-gridcell wake expansion. Also, based on prior numerical research (Pryor et al. 2018a), we anticipate

that wind farm wakes will be of greater magnitude and have most significant impact on near-surface climate during the summer season irrespective of the wind farm parameterization used.

b. WRF Model simulation

WRF has been extensively used within the climate community and wind energy industry. Version 3.8.1 is used here for a domain centered on the U.S. midwestern state of Iowa (Fig. 2). Iowa has the highest density of WT installed capacity of any state in the United States, and in 2014 had an installed capacity of over 5200 MW and thus an average installed capacity density of over 36 kW km^{-2} . To directly compare the two WT parameterization schemes, three identical inner domains (re-solved at 4 km) (no WT, WT Fitch, and WT EWP) are within the same coarser domain (12 km) run with no WT parameterization operating (Fig. 2). We apply the WT parameterization schemes in a yearlong simulation conducted for realistic WT densities that represent actual WT deployments. In an important advance over our past research (Pryor et al. 2018c) all inner domains that cover the same area and differ only in terms of whether a/which wind farm parameterization is employed are computed simultaneously within the identical outer domain. This minimizes potential impacts from

stochastic effects that may occur in independent simulations. The WT locations within Iowa as of the end of 2014 (Diffendorfer et al. 2015a,b; red symbols in Fig. 2) and WT type are used herein. As in previous research (Pryor et al. 2018a), the 20 most frequently used WT types were parameterized explicitly using the manufacturers' power and thrust curves while the remainder used average power curves scaled to the rated capacity for each WT. This gives a total of 3181 WT (98.9% of the total WT in Iowa) in the model domain. The outer model domain resolution of 12 km has 150×150 grid cells. The nested 4-km domain comprises 246×204 grid cells, and all three inner domains are operated without use of a cumulus scheme. This nested domain resolution captures atmospheric conditions over Iowa and surrounding midwestern states at high resolution and is also at a scale appropriate for operation of the WT parameterizations. There are 41 vertical levels up to a model top of 50 hPa; 18 of these levels are in the lowest 1 km of the atmosphere to suitably capture the PBL and the level of the atmosphere through which the WT rotor sweeps. WRF employs a sigma-level coordinate system, and thus the levels are not equidistant from the ground across the entire domain. However, as an example, in the wind farm cluster from which wake profiles are presented here, there are 10 levels in the lowest 370 m of the atmosphere (see profiles presented in section 3b).

The lateral boundary conditions are updated every 6 h from the ERA-Interim reanalysis data (Dee et al. 2011). Real-Time Global SST analyses (Reynolds and Chelton 2010) provide initial conditions for the Great Lakes and are updated daily. The key physics settings include the Eta Model microphysics scheme (Rogers et al. 2001), the Rapid Radiative Transfer scheme for longwave radiation (Mlawer et al. 1997) and the Dudhia scheme for shortwave radiation (Dudhia 1989), the revised Monin–Obukhov similarity scheme for the surface layer physics (Jiménez et al. 2012), the Noah land surface model (Chen and Dudhia 2001; Ek et al. 2003), and the Mellor–Yamada–Nakanishi–Niino PBL scheme (Nakanishi and Niino 2006); the Kain–Fritsch cumulus parameterization is used in the outer domain (Kain and Fritsch 1993).

The simulation presented herein starts with a month of spinup in November 2007, and output is presented here for the period 1 December 2007–1 December 2008. The year 2008 was selected because it is representative of the contemporary climate of the eastern United States. After a moderate La Niña in the first half of the year, ENSO-neutral conditions developed by July–August. In the continental United States, air temperature was only 0.1°C above the twentieth-century (1901–2000) mean (Pryor et al. 2018a).

Dynamic variables such as wind speed, along with generated power, are output and analyzed at 10 min intervals. Thermodynamic variables such as near-surface temperature, specific humidity, and sensible and latent heat are output once per hour.

c. Analysis

A comparison of the performance of the two wind farm parameterizations can be conducted for any arbitrary “wind climate” or near-surface conditions since it is the relative behavior of the two schemes that is of interest. Nevertheless, description of the specific atmospheric conditions provides context for the results presented herein, and an evaluation relative to the ERA5 reanalysis was undertaken (Copernicus Climate Change Service 2017; Hersbach and Dee 2016; Hoffmann et al. 2019). This reanalysis product was selected because it is unprecedented in terms of the data assimilated, represents the state of the art in terms of reanalysis model, and has output available at high spatial resolution. Note also that ERA5 is derived from the same “family” of models that generates the ERA-Interim output used to supply the lateral boundary conditions. Use of a reanalysis product for the simulation evaluation means that all points in the simulation domain are given equal weighting. For the near-surface atmospheric properties (air temperature and specific humidity at 2 m, along with sensible and latent heat fluxes), the evaluation relative to ERA5 and the effects from wind turbine operation focuses on the four climatological seasons: winter (December–February: DJF), spring (March–April: MAM), summer (June–August: JJA), and autumn (fall) (September–November: SON).

Given the importance of the wind regime to wind turbine wakes additional evaluation measures were employed. The WRF simulation of the flow conditions and electrical power production is evaluated using output from a high-resolution reanalysis product and in situ electrical power production estimates from operating wind farms. Evaluation of wind regimes from model simulations is particularly challenging in the context of wind energy relevant research due to the relative lack of publicly available wind observations above 10 m above ground level (AGL) and the high spatiotemporal variability of wind speeds (Pryor and Hahmann 2019). Evaluation of wind speeds from the inner domain operated without a wind farm parameterization operating is thus performed relative to output from the ERA5 dataset. The horizontal resolution of the ERA5 reanalysis is 30 km and key output variables include the U and V components of the wind at 10 and 100 m AGL. For the comparison with ERA5, the WRF Model output from the inner (4 km) domain is coarsened in both the

TABLE 1. Description of the wind farms in the Pomeroy study area (shown by the green dots in Fig. 2); RC = total wind farm rated capacity, IC = installed WT capacity, HH = hub height, and D = rotor diameter.

Project name	No. WT	Total RC (MW)	IC of WT (MW)	WT model	WT HH (m)	WT D (m)	Year online
Pocahontas Prairie	40	80	2	G90-2.0	100	90	2012
Pomeroy (Expansion)	13	29.9	2.3	SWT-2.3-101	80	101	2011
Pomeroy III	39	58.5	1.5	GE1.5-77	80	77	2008
Pomeroy II	49	73.5	1.5	GE1.5-77	80	77	2007
Pomeroy I	82	123	1.5	GE1.5-77	80	77	2007

time and space domains to match the resolution of ERA5. Thus, the 10-min output is first sampled once per hour for comparison with wind speeds at 10 m and once every 6 h for comparison at 100 m prior to averaging the results to the seasonal level. For the spatial remapping, the WRF output is averaged in each ERA5 grid cell. The resulting mean seasonal flow fields and near-surface climate variables from WRF (remapped to ERA5) and ERA5 are compared using Taylor diagrams that describe the ratio of the spatial standard deviations, the spatial correlation, and the root-mean-square deviation (Taylor 2001).

A further evaluation of the WRF output is performed by contextualizing gross capacity factors (CF) from the two wind farm parameterizations within estimated net CF for each calendar month in 2014–16 derived using net generation data as supplied in Energy Information Administration EIA-923 reports available from the U.S. Department of Energy ([U.S. Energy Information Administration 2000](#)) and total statewide installed capacity as reported in annual reports from the American Wind Energy Association ([AWEA 2014, 2015, 2016](#)). Note that net CF are computed only from wind farms that reported data for each calendar month of the given year to avoid biases due to commissioning of new wind farm arrays during the calendar year under consideration. It is important to note that gross CF are not equivalent to observed net CF for many reasons elaborated below. Comparison of the net and gross CF is used here to evaluate the degree to which the gross CF are plausible and whether they reflect the seasonal cycle of power production and thus wind regimes. Gross CF exceed observed net CF from operating wind farms because they assume 100% WT availability (i.e., no downtime for maintenance or curtailment of production) and neglect WT interactions within a grid cell (i.e., all WT in a WRF gridcell experience the same wind speed profile). These sources are estimated to reduce power production in the United States by <4% (curtailment) ([Pryor et al. 2018b](#)), <2% (operations and maintenance) ([Carroll et al. 2017](#)), and $\leq 5\%$ (within wind farm wakes) ([Staid et al. 2018](#)). Thus, the discrepancy between net and gross CF varies in time and space, but

these factors are likely to be on the order of a few percent (i.e., in the absence of other errors, if estimated gross CF is 40%, net CF are likely to be in the range of 30%–36%). Further, internal climate variability induces considerable intra and interannual variability in wind speeds and thus electrical power production (and CF). A recent analysis of the variability in gross annual energy production (AEP) across the eastern United States indicated that over Iowa the 25th–75th-percentile range of AEP estimated using modeled wind speeds and an average WT power curve is approximately 3%–5% of the median value ([Pryor et al. 2018b](#)). Thus, while some of the intra- and interannual variability in statewide net CF reported herein may reflect errors/omissions in the EIA-923 reports, variability of the wind climate provides an additional important caveat to comparison of modeled gross CF for the climate of 2008 and net CF for 2014–16 computed as described above.

The effects of WT arrays on electrical power output (expressed as CF) and atmospheric conditions at the local to regional scale are quantified using pairwise (in time and space) comparison of output from the domains in which the wind parameterizations are operational (d03 for Fitch and d04 for EWP) versus the domain with no WT operating (d02). The characterization of the downstream recovery distances for wind farm wakes is illustrated using examples drawn from a large multiarray (i.e., multiple wind farm) area in Iowa. This study area located in west-central Iowa (referred to herein as the Pomeroy study area) actually comprises five developments that are described in [Table 1](#). To examine the degree to which wind farm effects on near-surface climate properties are expressed at the local or regional scale, the impact on grid cells containing WT (shown in red in [Fig. 2](#)) is compared with mean pairwise differences in an equal number of randomly selected background grid cells located at least six grid cells from the closest WT (shown in black in [Fig. 2](#)).

A two-sample *t* test is applied to test the statistical significance of mean pairwise differences in each variable in each grid cell for each season and each of the two wind farm parameterizations versus the no-WT output.

This statistical test is applied to test the hypothesis that samples of hourly near-surface air temperature, specific humidity, and sensible and latent heat fluxes or 10-min wind speeds from the Fitch or EWP domains and those from the no-WT domain derive from Gaussian distributions with equal means and equal (but unknown) variances. A significance level α of 0.01 is employed to detect statistical significance. For each field (season, variable, and wind farm parameterization) the statistical test is applied 246×204 (i.e., 50184) times. This leads to substantial familywise error rates (or alternatively stated a high probability of false discovery) (Wilks 2011). Hence, the results are corrected for multiplicity by ranking the p values from each of the grid cell (where $j = 1$ is allocated to the smallest p value and k is the total number of grid cells) and then selecting as statistically significant only those for which the following condition is realized (Wilks 2011):

$$p_j \leq \frac{j}{k} \alpha. \quad (5)$$

Empirical quantile–quantile plots are used to examine the probability distributions of near-surface climate variables from d02 versus d03 and d04 in grid cells with WT and those from the background grid cells.

3. Results

a. 2008 conditions as simulated by WRF

Consistent with the observed seasonality of estimated net CF shown in Table 2, there are marked intra-annual (seasonal) simulated wind speeds over the inner domain (d02) operated without the effects of WT (Figs. 3a and 4). The seasonal cycle is characterized by stronger wind speeds in spring/fall, with more moderate speeds in winter months, and calmer summer months. The mean wind speed (Fig. 4) also illustrates that even for a relatively flat state such as Iowa (see Fig. 2 for elevation), the effects of topography are still present. Such effects are evident when comparing the elevation in Fig. 2 with the seasonal wind speed in Fig. 4, which shows areas of wind speed variability associated with up/downslope winds across terrain and/or valleys. This adds to the complexity in diagnosing and characterizing wind farm wakes. Thus, herein wind farm wakes are characterized using a velocity deficit computed pairwise in time and space between output from domain 2 (the no-WT domain, d02) and output from the domains in which Fitch and EWP wind farm parameterizations are operating (d03 and d04, respectively).

The wind regimes during 2008 from WRF over the inner domain (d02) is positively biased relative to ERA5.

TABLE 2. Gross capacity factors (CF) as computed from the domains employing the Fitch and EWP wind farm parameterizations by month and season for all WT in Iowa. Also shown are the net CF derived for each calendar month in 2014–16 derived using net generation data as supplied in EIA-923 reports available from the U.S. Department of Energy Energy Information Administration ([U.S. Energy Information Administration 2000](#)) and total statewide installed capacity from American Wind Energy Association annual reports ([AWEA 2014, 2015, 2016](#)).

	Gross CF from simulation		Net CF from observed electrical power generation and installed capacity		
	Fitch	EWP	2014	2015	2016
Calendar month					
Dec (2007)	41.8	44.9	34.1	38.7	47.8
Jan (2008)	53.9	57.1	48.1	42.9	37.6
Feb	40.9	43.6	38.0	41.4	45.4
Mar	43.8	46.1	45.0	39.0	42
Apr	55.5	56.3	47.3	39.2	52.4
May	50.6	52.2	32.8	38.0	28.9
Jun	39.6	41.5	27.6	22.1	29.3
Jul	31.5	33.8	23.8	18.3	21.3
Aug	38.0	41.1	13.9	23.0	17.1
Sep	41.8	44.3	25.6	31.1	34.4
Oct	50.8	52.8	37.0	37.4	37.3
Nov	54.1	56.6	50.8	45.8	42.8
Season					
DJF	42.1	44.9			
MAM	48.7	50.3			
JJA	36.7	39.6			
SON	50.5	52.9			

The seasonal mean wind speeds from WRF at nominal heights of 100 and 10 m AGL are positively biased for all seasons, irrespective of whether the WRF output is remapped to the ERA5 grid (Fig. 4a). The Taylor diagram indicates that mean spatial fields of wind speeds from ERA5 and WRF exhibit positive spatial correlations in all seasons and similar ratio of spatial standard deviations (Fig. 4b), although when WRF is remapped to the resolution of ERA5, the spatial variability appears to be underestimated in output at both 10 and 100 m. The discrepancies between the ERA5 reanalysis output and WRF also vary seasonally. The bias in the mean wind speed is larger in summer (Fig. 4), consistent with the greatest discrepancy between gross CF and net estimated observed CF during this season (Table 2). This seasonality in differences between WRF and ERA5 output may reflect differences in the stability climate, given that the lateral boundary conditions are supplied from a reanalysis dataset and thus should represent the synoptic scale with substantial fidelity.

An important caveat to the apparent overestimation of 100 m AGL wind speeds in the WRF simulations

presented here is that if the mean wind speed from WRF output over Iowa at 100 m AGL is extrapolated to 80 m using the logarithmic wind profile and a surface roughness length of 0.1 m, the estimate of 7.9 m s^{-1} exhibits relatively good agreement with estimates of the annual mean wind speed at 80 m over Iowa [data produced by AWS Truepower LLC (2010) for U.S. Department of Energy] of approximately 7.5 m s^{-1} , whereas the domain-averaged mean wind speed at 80 m AGL derived in the same way from ERA5 is 5.9 m s^{-1} . Thus, some fraction of the discrepancy evident in Fig. 4a may also be attributable to negative bias in ERA5. Negative bias in ERA5 wind speeds close to 100 m AGL has also been reported in previous research comparisons relative to WRF (Pryor et al. 2020) and in situ observations (A. Hahmann, Technical University of Denmark, 2019, personal communication). ERA5 wind speeds are less negatively biased than MERRA-2 over Sweden but are still negatively biased relative to wind speed estimates derived from wind turbine power production data (Olauson 2018). Over the North Sea, ERA5 wind speeds also exhibit a negative bias in the mean relative to observations (Kalverla et al. 2019). However, it is also possible that the difference in wind regimes is a function of positive bias in the WRF simulations. Evidence of positive bias in wind speeds in high-resolution simulations with WRF have also been reported at locations over northern Europe (even offshore) and have been shown to vary with the PBL scheme applied in the model (Draxl et al. 2014; Hahmann et al. 2015; Pryor and Hahmann 2019). These biases are of great importance to estimation of wind resources and provide an important context for the wake behaviors described here. However, the differences between wind farm wakes as represented in simulations with EWP and Fitch should be relatively insensitive to biases in the inflow wind speed from WRF.

For the other simulated atmospheric variables analyzed herein, as shown in Fig. 4c, the spatial patterns of near-surface air temperature and specific humidity (derived for ERA5 from the 2-m dewpoint temperature and surface pressure) are generally in good agreement in all seasons [spatial correlations of > 0.8 except for specific humidity in summer (0.58)]. In general, the output from WRF exhibits higher spatial variability ($\sigma_{\text{WRF}}/\sigma_{\text{ERA}} > 1$). There is considerably less good agreement for the two surface energy fluxes, particularly during summer. ERA5 exhibits much higher summertime sensible heat fluxes than latent heat fluxes over the entire WRF inner domain, while the converse is true of WRF. This may be partly attributable to a reported positive bias in ERA5 soil moisture relative to satellite observations (by a factor of >2) that has recently been

reported for the upper central plains of North America and locations in Europe (Piles et al. 2019).

Wind roses for a representative grid cell located in Missouri (see cyan marker in Fig. 2 for location), indicate important seasonality in prevailing wind direction (Fig. 5). Given the locations of major WT arrays in Iowa is highly irregular, there is marked seasonality in the potential for array–array interactions. While flow is generally oriented along an east–west axis in winter, the wind rose is illustrative of predominantly southwest flow in summer (Fig. 5). In the fall, flow is predominantly from the west, and greater variability prevails in spring months. The wind roses indicate that distant from WT arrays the impact from even the dense WT deployments in Iowa is very modest. In winter months, there is negligible difference between no WT and either Fitch or EWP (Figs. 5a,b). The fraction of winds from an easterly direction is roughly 0.5%–1% greater in EWP than in Fitch; otherwise the wind regime is identical. During summer months, however, there is a difference in the frequency of winds from the prevailing southwesterly direction between the two cases. EWP shows a 0.5% increase in frequency of southwest winds relative to Fitch (Figs. 5h,i).

b. Wind farm wakes as simulated using EWP and Fitch

Figure 6 shows the seasonal mean wind speed difference (at approximately 100 m AGL) computed from gridcell-specific pairwise differences in wind speeds from d03 and d04 versus the domain in which no wind farm parameterization is included (d02). As shown, while the average impact on wind speed has a maximum value in any individual grid cell of -0.7 m s^{-1} , the largest impacts on wind speed are observed in the summer months. Further, there is a systematic bias of more intense near-field wind farm wakes from the Fitch parameterization (Fig. 6). The seasonality in the wake intensity and downstream propagation is a complex function of 1) seasonality in wind speeds and thus the thrust coefficient (Fig. 3b) that dictate the initial wake generation, and 2) seasonality in wind directions that dictate the potential for wakes to propagate over nearby WT arrays (Fig. 5). It is further dictated by wake recovery rates that are determined by the stability conditions and ambient turbulence intensity that control the rate at which momentum can be transferred into the wake to reduce the velocity deficit. The more intense wakes during summer are likely dominated by the former effect—that a greater frequency of lower wind speeds (Fig. 3a) means the WT are generally operating with higher thrust coefficients (Fig. 3b) that generate more intense wakes. During winter the probability

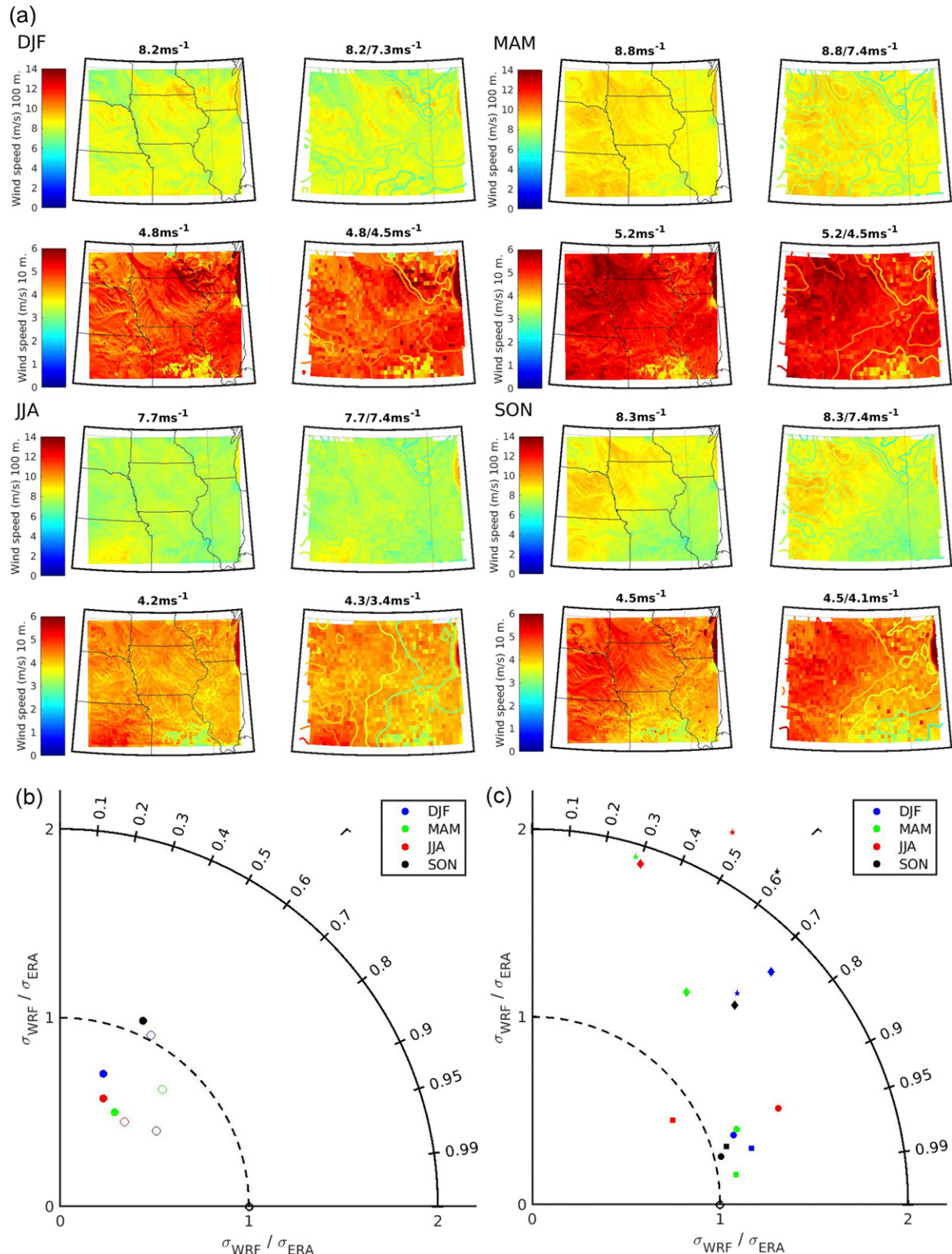


FIG. 4. (a) WRF wind speed evaluated against ERA5 reanalyses for each season as labeled to the upper left of the groups of four plots. The top two plots of a group show the seasonal mean wind speed at 100 m, and the bottom two plots show 10-m wind speed for WRF at the original resolution (left two plots) and remapped to the ERA5 resolution (right two plots), with ERA5 wind speed contoured. Above each plot is a single value indicating the spatially averaged mean wind speed for the entire domain (the slash in the right-hand plots separates

distribution of wind speeds is shifted right indicating generally lower thrust coefficients (Fig. 3). This effect is partially offset by the fact that stable conditions and low turbulence intensity, which retard vertical momentum transport, are more common in winter. In spring and fall, when the wind speeds are higher (Fig. 3a), the WT operate more efficiently (thrust coefficient is lower Fig. 3b), and thus weaker wakes are generated and propagated downstream. In summer there is some evidence of statistically significant perturbations to the flow climate distant from wind farms with patches of increased and decreased wind speed throughout in the inner domain (Fig. 6). These are not evident in other seasons. This effect may potentially be the result of enhanced vertical coupling and momentum transfer, due in part to the change in sensible heat and TKE introduced by the WT parameterization and mixed away downstream by the PBL scheme. This, however, requires further quantification over longer time scales, because if such an effect were operating, we would expect to see domainwide feedback during winter months, when wind farm wakes are similar to those manifest in summer.

To further illustrate the differences in near-array wake characteristics and the downstream propagation and recovery we present composite vertical profiles from the Pomeroy cluster of wind farm arrays (shown by green symbols in Fig. 2). Most previous analyses that have presented downstream profiles of velocity deficit downstream of WT arrays have focused on idealized cases (Miller et al. 2015) or wind farms with a single WT height deployed in a regular array (Volker et al. 2015). The Pomeroy area of Iowa comprises five different projects (Table 1) and thus reflects a more typical situation where multiple arrays are developed within relatively close proximity. In this analysis pairwise profiles of wind speeds from d02 and d03 or d04 are used to compute velocity deficits [i.e., $v_d(x, y, z, t) = WS(x, y, z, t)_{d03}$ minus $WS(x, y, z, t)_{d02}$, where x and y are the gridcell locations, z is the vertical level, and t is the time stamp of that 10-min period]. The resulting data sample is used to compute the median and interquartile range of those individual velocity deficit values at each x, y, z position. This analysis is presented for two transects, one crossing the western side of the wind farm cluster and thus traversing the densest part of the array, and the other over the eastern portion of the wind farm cluster

(Figs. 7 and 8). Along the western transect the density of installed capacity is $\sim 4 \text{ MW km}^{-2}$ (275 MW is deployed in arrays that cover a total area of 66.5 km^2). The eastern portion of the development (Pocahontas Prairie Project) is sparser and more irregular. The total installed capacity is 80 MW over a highly irregular polygon with an approximate area of $> 30 \text{ km}^2$. The density of installed capacity along the eastern transect is less than one-half that on the western transect. As indicated by Fig. 2 and shown in Fig. 9, there are major WT arrays located to the south and west of the Pomeroy cluster; therefore, the northerly sector was selected for these illustrative case studies to reduce disruptions on the inflow wind profile from other upstream arrays.

Illustrative composite profiles showing the median and interquartile range of all 169 cases of northerly airflow (i.e., wind direction of 355° – 5°) during which the total power produced by this cluster was 50%–75% of the total rated capacity according to both EWP and Fitch are given in Figs. 7 and 8. On both transects the freestream flow in one grid cell upwind (i.e., 4 km) of the wind farm location (first profile in Figs. 7a and 8a) is virtually identical in d02 (no WT), d03 (Fitch), and d04 (EWP). For the transect through the higher installed capacity (the western transect) across the rotor plane (approximately 41.5–118.5 m AGL) the median absolute velocity deficit in the WT grid cells operating the Fitch scheme exhibit values of up to 3.5 m s^{-1} , whereas those from EWP are $< 2.5 \text{ m s}^{-1}$. The velocity deficit for the upper 25% of these wake cases exceeds 6 m s^{-1} in simulations with Fitch but is below 4 m s^{-1} in EWP (Figs. 7a,b). On the eastern transect the velocity deficits are much lower (Fig. 8) and the median absolute velocity deficits within the wind farm are less than 2.5 m s^{-1} in Fitch and less than 1.5 m s^{-1} for EWP. These differences within the grid cells that cover the wind farms is a direct result of the different physical formulations of wind farm parameterizations and specifically the within-gridcell treatment of wake expansion in EWP. This effect is less pronounced in the downstream grid cells, where the addition of TKE in the Fitch scheme enhances the wake expansion and recovery. The downstream distance at which the wake is no longer discernible is defined as the distance at which the median velocity deficit at every point in the profile is $< 0.2 \text{ m s}^{-1}$. This is approximately seven downstream grid cells (24–28 km from the edge of the array) for the western transect and 6 (20–24 km) for

←

the spatially averaged mean wind speed for the original resolution and for the remapped resolution). (b) Taylor diagram of seasonal mean wind speed at 100 (solid circles) and 10 (open circles) m. (c) Taylor diagram of seasonal mean air temperature at 2 m (squares), latent heat (diamonds), sensible heat (stars), and specific humidity at 2 m (circles) from WRF and ERA5.

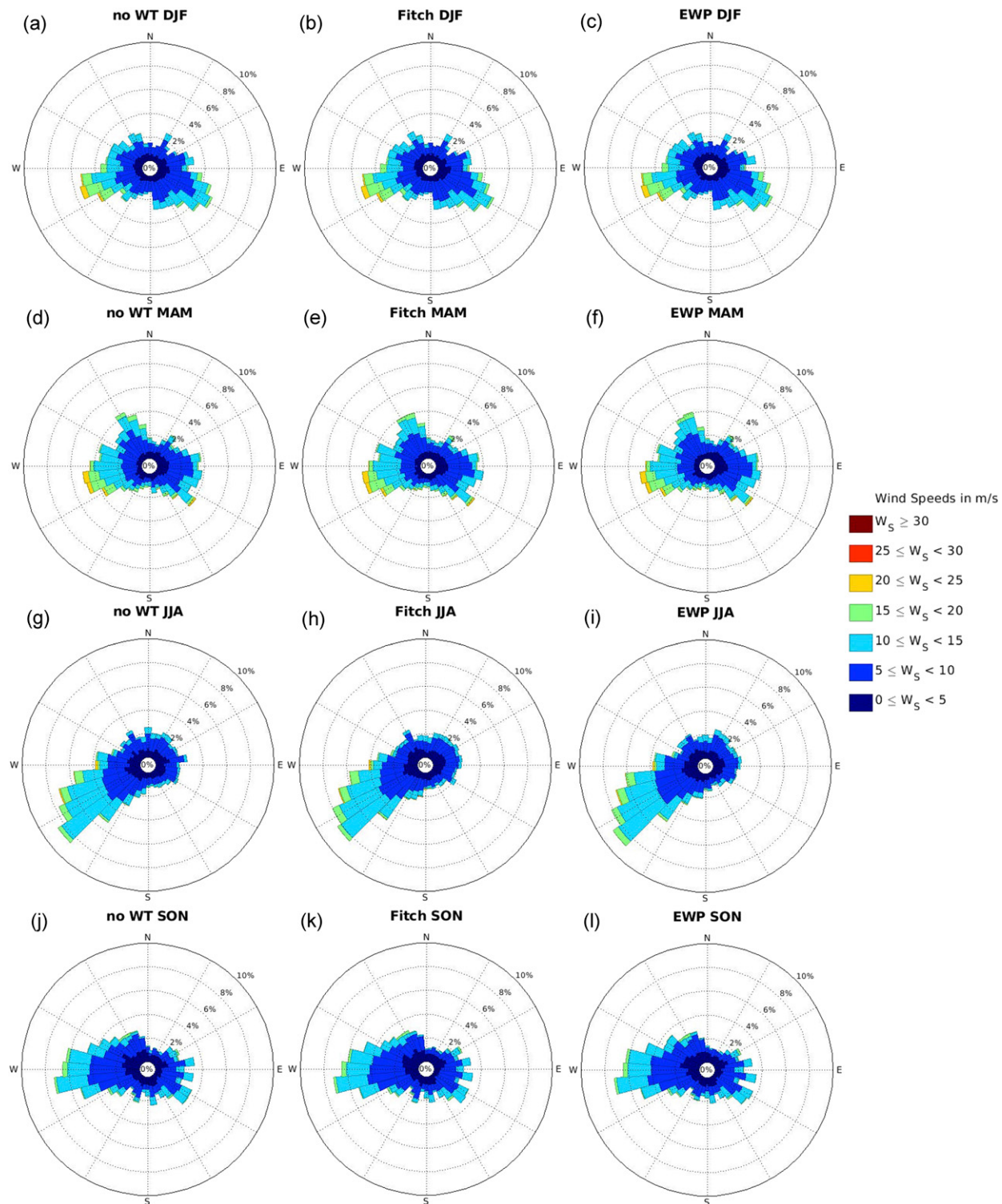


FIG. 5. Seasonal wind roses of all 10-min wind speed and direction for a grid cell located in Missouri (see cyan marker in Fig. 2 for location) for ~ 100 m AGL (i.e., close to typical WT HH). The roses are grouped by season [(a)–(c) December 2007–February 2008, etc.] and show the wind regime from the (left) no-WT, (center) Fitch, and (right) EWP domains.

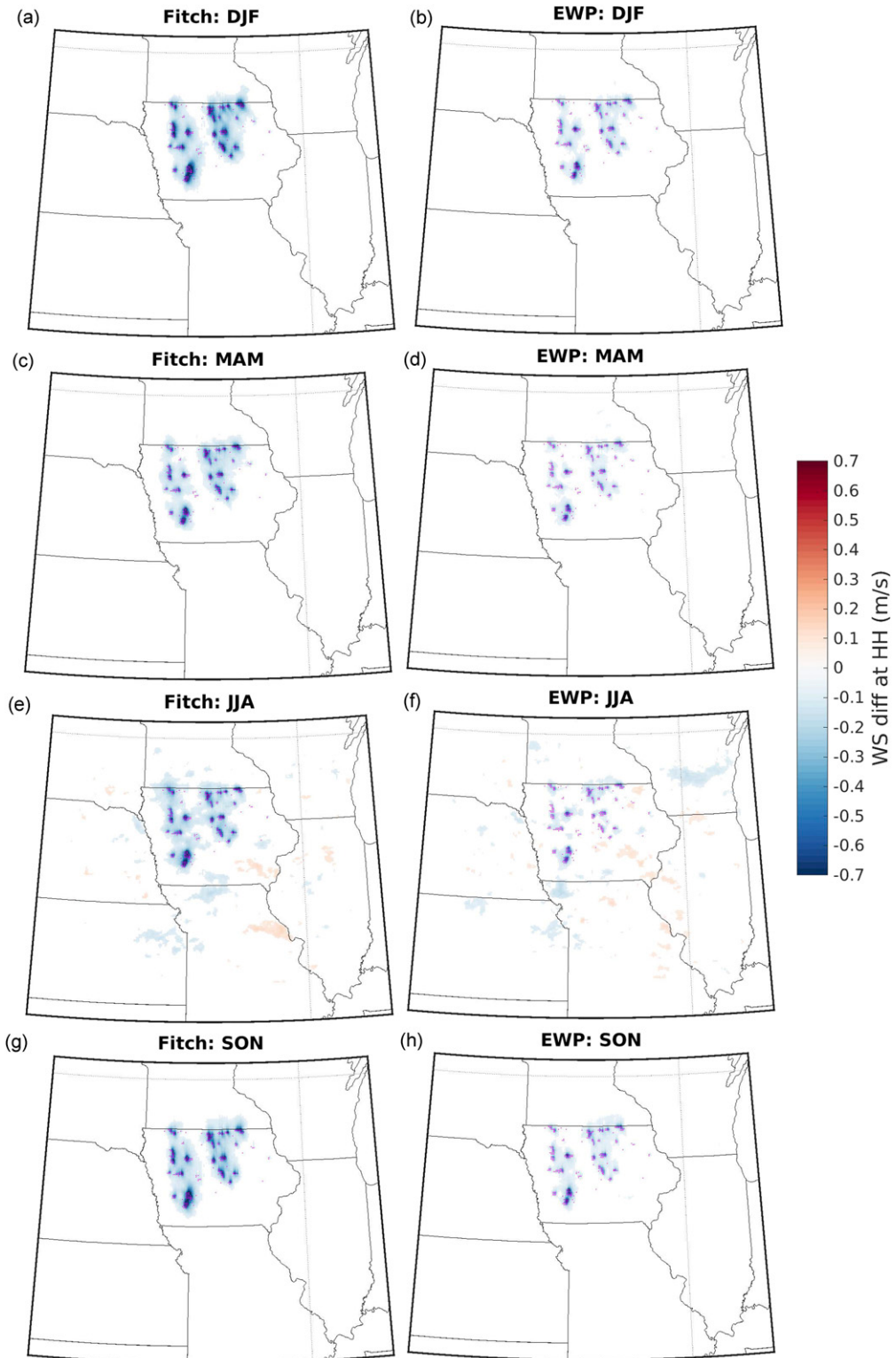


FIG. 6. Seasonal (by row) mean pairwise difference in wind speed at ~ 100 m AGL (third model layer, close to the mean WT HH) for all grid cells in the inner nest (4 km) in simulations using (a),(c),(e),(g) Fitch and (b),(d),(f),(h) EWP vs d02 (no WT). The magenta dots represent grid cells in Iowa that contain WT. Differences are only shown for grid cells for which a two-sample t test indicated that the mean values derived from samples from the wind parameterization domain and the no-WT domain were significantly different.

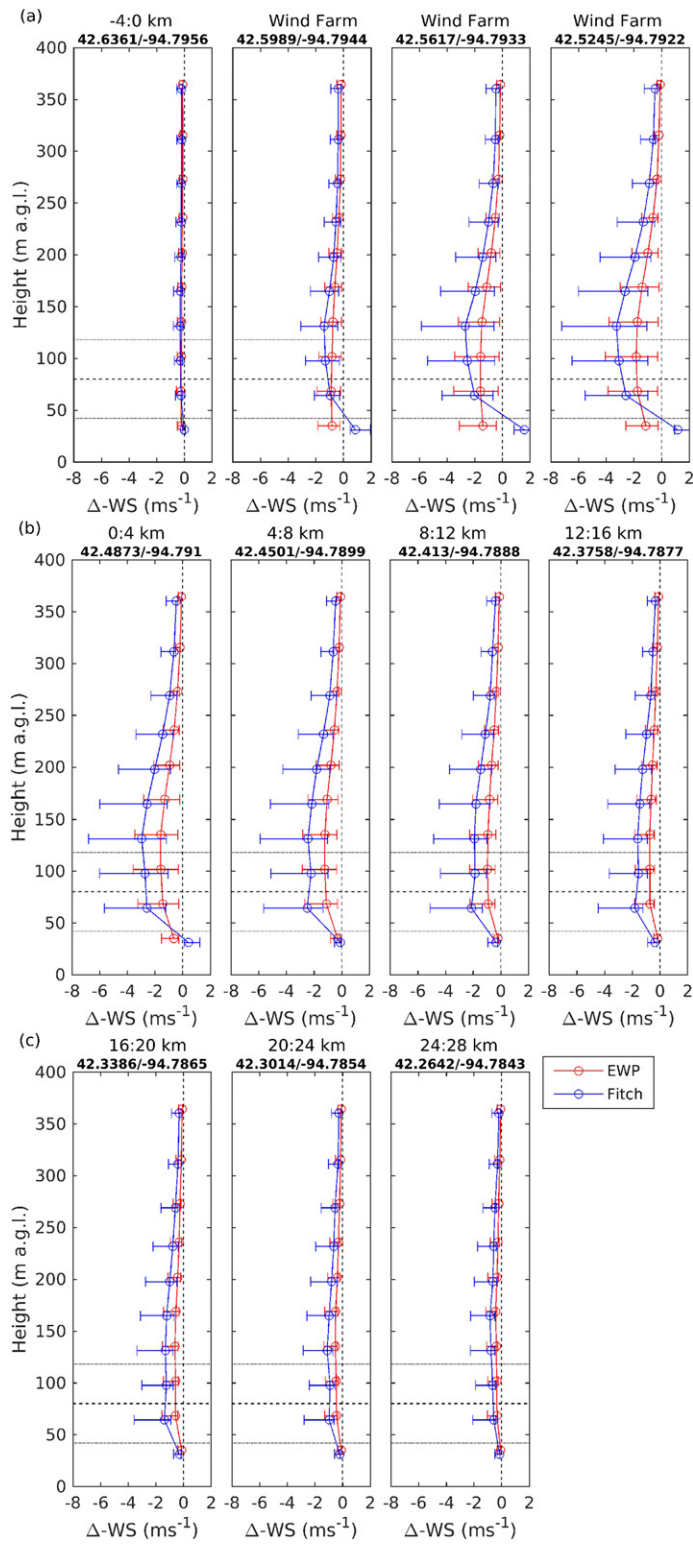


FIG. 7. Vertical profiles of the median and interquartile range of velocity deficit [Δ -WS, where the pairwise values are computed as $WS(x, y, z)$ from d03 or d04 minus $WS(x, y, z)$ from d02] for a western transect over the Pomeroy wind farm site (Table 1). The horizontal dotted line represents

the eastern transect in simulations with both EWP and Fitch (Figs. 7 and 8). At every intervening downstream distance, however, the wake velocity deficit is smaller in the simulations with EWP. The third feature that is evident from these profiles is the lofting of the wake center from the WT HH due to the vertical allocation of the drag within the Fitch scheme. This effect is even more pronounced in the downstream grid cells. A final difference between the two schemes is that there is an increase in wind speed at the lowest model level in the domain with Fitch relative to the no-WT domain. As shown below, this acceleration of flow in the lowest model layers in Fitch relative to EWP has implications for the near-surface climate impacts.

As further illustration of the difference in wake characteristics and downstream propagation in simulations with Fitch and EWP, Fig. 9 shows horizontal planes of velocity deficit from the third model layer (~ 100 m AGL) in the vicinity of the Pomeroy WT clusters. The velocity deficits for each of the 169 northerly cases are normalized to the wind speeds in each grid cell from the no-WT domain (d02) for the same time stamp and grid location. Thus, the velocity deficit is normalized, where a value of -0.05 indicates the wind speed is an average of 5% lower in the d03 or d04 output than in the output from d02. On the western transect in the southernmost grid cell located within the WT array the mean normalized velocity deficit is 20%, while in EWP it is 13.6%. Consistent with depictions in Figs. 7 and 8, this analysis shows the higher intensity of the wakes from simulations with Fitch and indeed suggests that if a deficit magnitude of 5% is used to indicate the edge of the wake or the separation of wind arrays necessary to have “minimal” wind theft, this separation distance is shorter in the domain with EWP. For this case study it is achieved after two grid cells downstream from the edge of WT array in the western transect in EWP and three in Fitch. However, if a different criterion is used, for example, a recovery of the wakes such that the mean velocity deficit is $<2\%$, both schemes indicate the recovery is at five downstream grid cells. Thus, the downstream recovery distance and the implications for optimal locations of new deployments in the shadow of existing development is highly dependent on the acceptable level of wind theft

and the prevailing wind climate (frequency of power producing wind speeds from a specific wind direction).

Differences in TKE from the two wind farm parameterizations for the transect over western Pomeroy (Fig. 10) indicate the following: 1) TKE is greatly enhanced over the wind farm in all model levels shown in simulations with Fitch because of the production of TKE from the action of WTs (consistent with the discussion in section 2). 2) In grid cells containing WTs, TKE is reduced in the lower model layers in the EWP scheme as a result of the extraction of kinetic energy but is slightly enhanced above the WT rotor plane because of the increase in shear. 3) With increasing downstream distance, the TKE profiles from the two schemes become increasingly similar. Both show a weak region of enhanced TKE elevated from the wind turbine upper rotor tip and decreased TKE closer to the surface.

c. Systemwide efficiency

The differences in wake effects illustrated in section 3b have implications for array–array interactions and thus power generation across individual wind farm clusters and indeed the entire system of WT in Iowa. The accumulated annual power production over all WT in Iowa is over 1 TWh higher in the domain with EWP than from the domain in which Fitch was operating (Fig. 11). Thus, the EWP scheme implies lower array–array interactions that result in a systemwide increase in total annual power production of 5%. The impact on the systemwide efficiency of electrical power generation, as expressed using monthly and seasonal gross CF, indicates higher values in all calendar months and all seasons in the domain with EWP operating (Table 2). During summer months, when the mean wind speed (WS) differences (Fig. 6) are largest, the enhancement of systemwide efficiency in EWP relative to Fitch results in CFs that are consistently 2%–3% higher than those from Fitch.

The actual cumulative total number of TW h of electricity generation from WT in Iowa during 2014 as reported by the U.S. Energy Information Administration (2015) was approximately 16.3 TW h. Simulated gross total number of TW h of electricity generation from the WT in Iowa deployed during 2014 but for the wind



the WT hub height, and the horizontal lines above and below it indicate the rotor-swept area. The vertical coordinate used to display the profiles of velocity deficit from EWP and Fitch has been slightly offset (by ± 2 m) from the actual gridcell level to aid legibility. The values above each plot show the centroid of the grid cell (latitude/longitude) and the distance upstream or downstream of the wind farm.

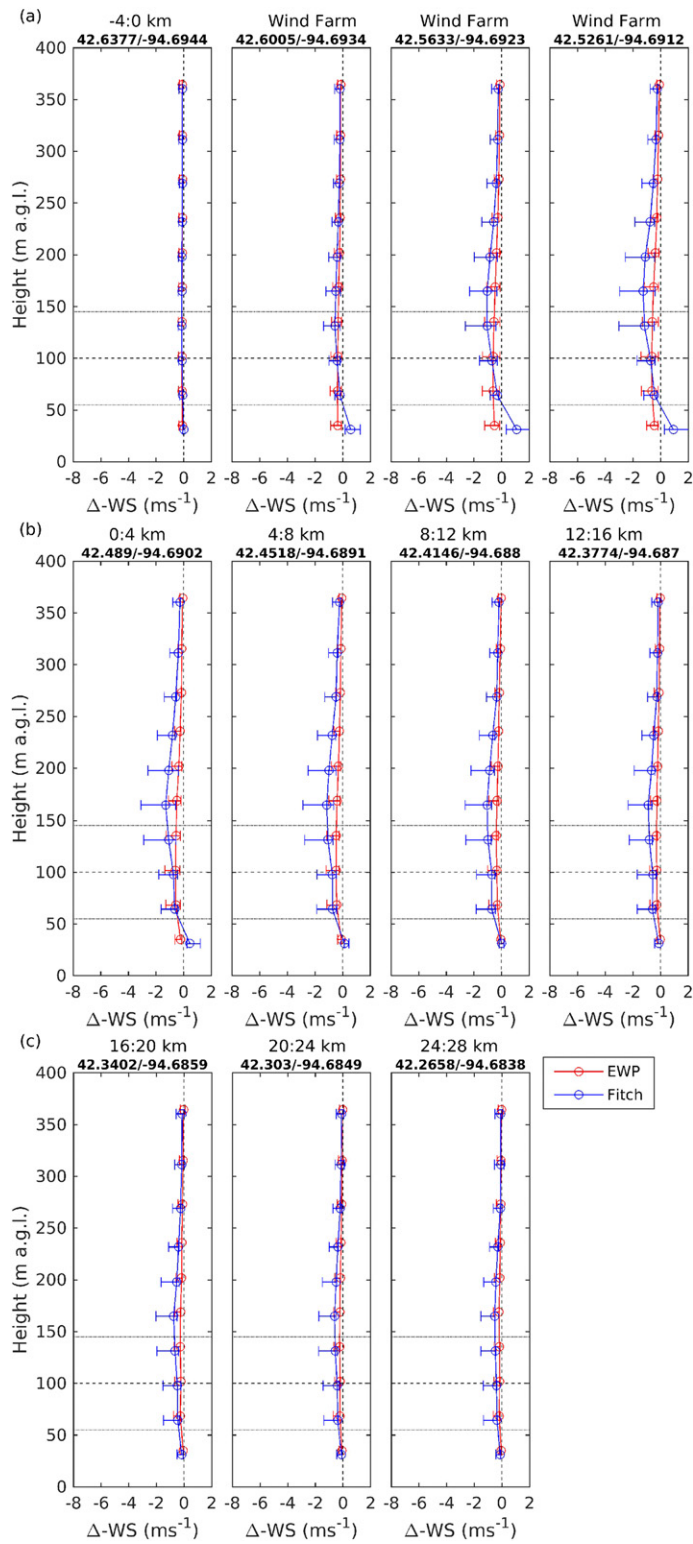


FIG. 8. As in Fig. 7, but for the Pocahontas Prairie wind farm transect.

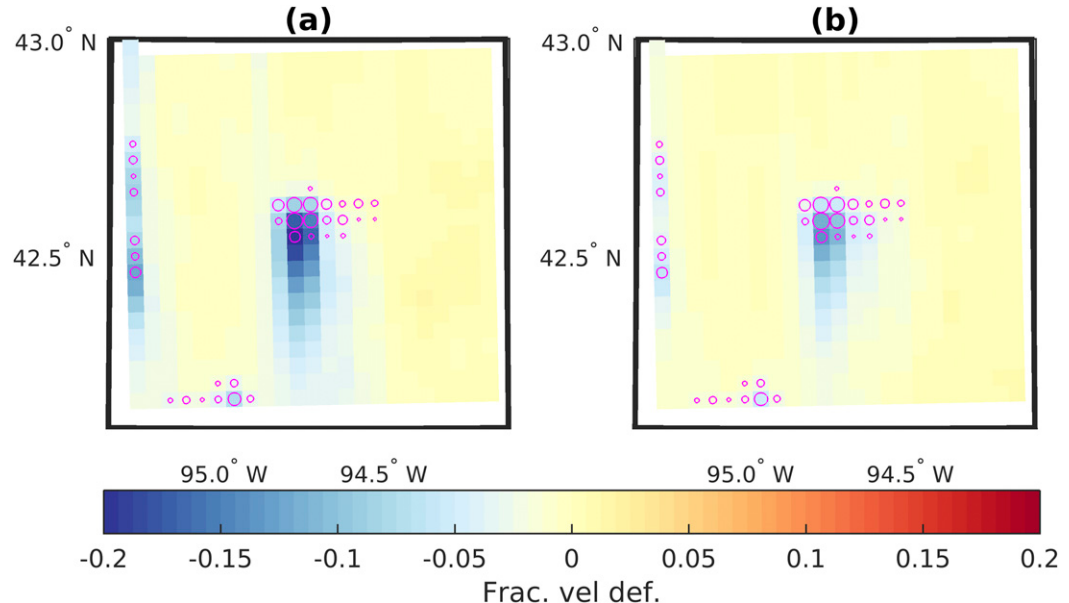


FIG. 9. Mean normalized (fractional) velocity deficit [i.e., $\{WS(x, y, 3)_{d03} - WS(x, y, 3)_{d02}\}/WS(x, y, 3)_{d02}\}$] at the wind farm cluster for (a) Fitch and (b) EWP from the third model layer (~ 100 m AGL). The mean is derived from fractional velocity deficits in 169 northerly wind cases used for the vertical profiles in Figs. 7 and 8. The installed capacity (IC) in each 4-km grid cell is shown by the magenta circles that scale in diameter with increasing IC.

climate of 2008 as derived from simulations with Fitch and EWP are 20.1 and 21.1 TW h, respectively (Fig. 11). This difference is due to interannual variability in the wind climate and also exclusion of power losses due to factors such as electrical losses, operations and maintenance, and near-wake effects, and to the biases in wind speeds described in section 3a. Although all calendar months exhibit higher simulated gross power production from EWP than Fitch, the discrepancies are unevenly distributed across the simulation period. This is illustrated in Fig. 11, which shows the accumulated gross electrical power production, accumulated power difference and accumulated difference rate from Fitch and EWP as a function of day of the simulation. The largest differences in gross daily power production from WT in Iowa is observed in December 2007 and January 2008, and it is minimized in April 2008. This is consistent with the operation of WT [i.e., highest mean wind speeds (Fig. 3a) mean the WT are operating most efficiently], and thus the thrust coefficients are lower and the wake effects from both parameterizations are smaller.

d. Impacts from WT array on near-surface climate variables

Consistent with previous research using the Fitch wind farm parameterization over the Midwest (Pryor et al. 2018a), the impact from WT on local and regional temperature at 2 m AGL from both wind farm schemes

is modest. Close to WT arrays, 2 m AGL temperature is generally enhanced in winter and fall in output from the Fitch wind farm parameterization (Fig. 12). There are also some remote effects during summer. Impacts on near-surface temperatures are much more modest in simulations with EWP. The effects are not completely symmetric about zero and generally are of largest magnitude close to WT arrays. Areas with nonzero differences are widely spatially distributed across the domain in summer, which may indicate the presence of stochastic effects arising from numerical uncertainty. These areas may also represent compensating effects throughout the model domain caused by changes in turbulence levels and PBL dynamics. Alternative explanations invoking chaos seeding (Hacker et al. 2017) can likely be discounted since such perturbations would begin at $t = 0$ and grow throughout the simulation time period. If such random perturbation from noise were to have occurred, the result for spring months (Figs. 12g,h) would show large model noise, but here we find no such effect. Indeed, the climate impact for spring months is generally less than 0.05 K in both EWP and Fitch.

The maximum mean temperature differences ($d03$ or $d04$ minus $d02$) in any grid cell from both the Fitch and EWP schemes range between -0.68 and $+0.57$ K (Fitch) and -0.53 and $+0.65$ K (EWP) and occurs in June–August. This temperature difference tends to occur in the vicinity of larger WT arrays in Iowa, while

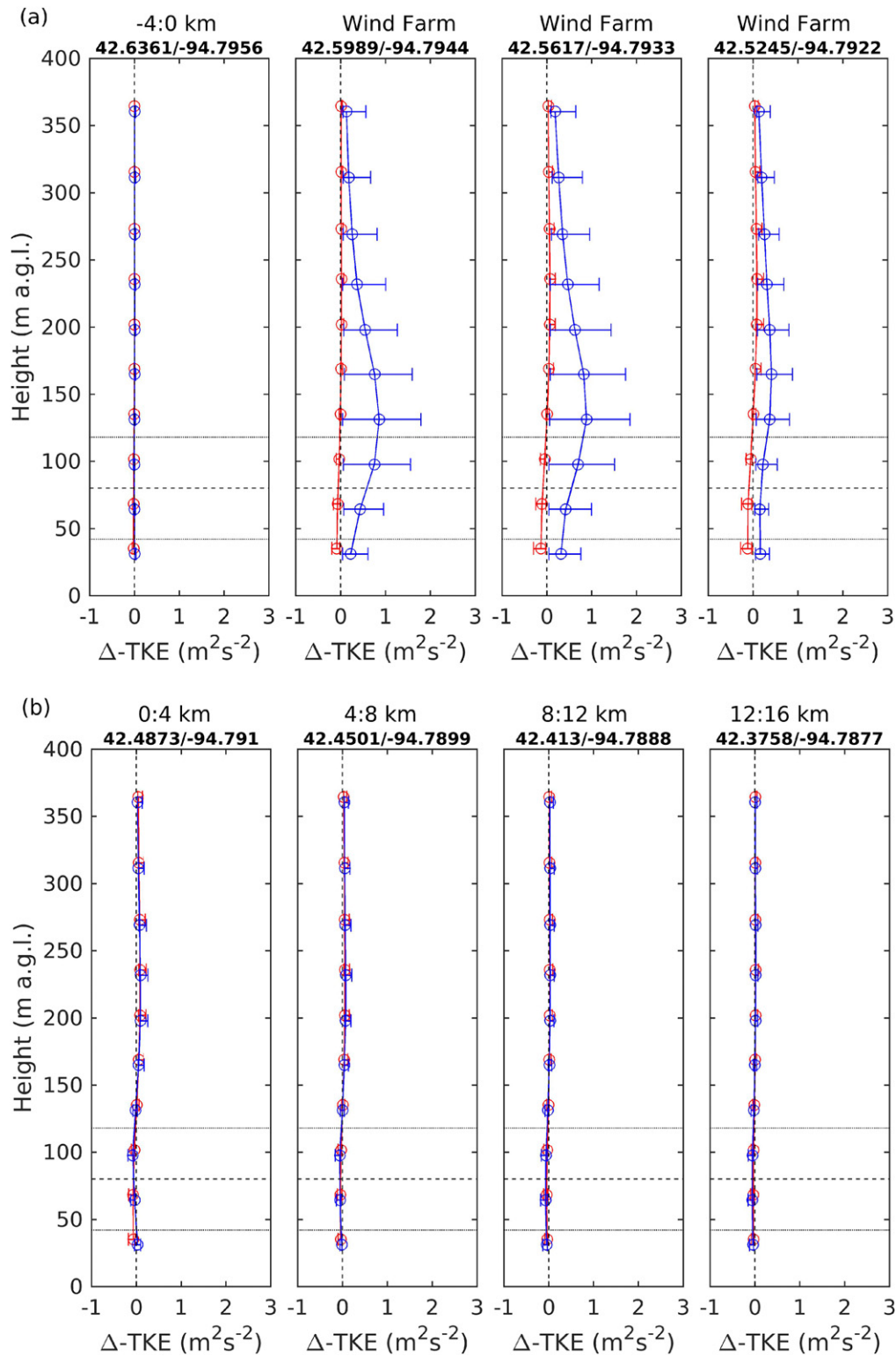


FIG. 10. As in Fig. 7, but for the difference in TKE in the two wind farm parameterizations relative to the no-WT output [$\Delta\text{-TKE}$, where the pairwise values are computed as $\text{TKE}(x, y, z)$ from d03 or d04 minus $\text{TKE}(x, y, z)$ from d02].

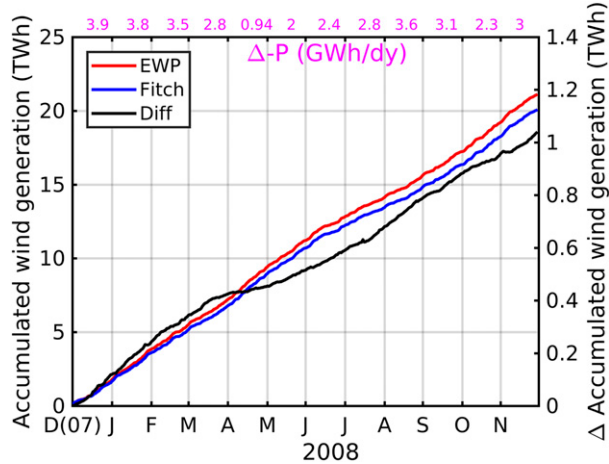


FIG. 11. Accumulated daily wind generation in TWh for Fitch (blue) and EWP (red) over the simulation period derived using all 10-min power output for each scheme from the 4-km inner nest. The accumulated difference in wind generated electricity is shown in black. The difference in power accumulation rate (GW h day^{-1}) for each month is shown along the top axis.

the smaller WT arrays show smaller climate impacts. Pairwise comparison between the no-WT and Fitch domains shows that the temperature in and near large WT arrays tends on average to be warmer than in the no-WT case, consistent with previous research (Xia et al. 2019). This warming effect is of smaller magnitude and/or of opposite sign in the domain with EWP. Temperature differences in the present study are similar to estimates derived from land surface temperature data derived from Moderate Resolution Imaging Spectroradiometer (MODIS) on the *Terra* and *Aqua* satellites (Harris et al. 2014), but they are of smaller magnitude in part because MODIS data are confined to cloud-free conditions.

Empirical quantile–quantile (EQQ) plots of 2 m AGL temperature from Fitch and EWP versus no WT indicate warming of the coldest hours in grid cells containing WT particularly in winter and summer when either wind farm parameterization is employed (Fig. 13). The magnitude of this effect is larger in Fitch but consistent across both wind farm schemes in winter likely from enhancement of mixing in the lower atmosphere and entrainment of warmer air from aloft. The amplification of near-surface warming in simulations with the Fitch scheme relative to EWP appears to be that the stronger low-level shear in Fitch (see Figs. 7 and 8) is associated with enhanced nocturnal mixing and suppression of near-surface cooling. The larger magnitude of this effect in Fitch during the winter months (Fig. 13) and the greater spatial scale of effects is consistent with the more intense wakes and

acceleration of flow close the ground (Figs. 7 and 8). In the background grid cells, the EQQ plots indicate virtually no difference between the output from d03 and d04 and that from d02, indicating that the effects from WT on near-surface air temperature is localized to the grid cells that contain WT.

Similar spatial maps of the mean pairwise temperature perturbations from Fitch and EWP for other near-surface climate properties—sensible heat (SH), latent heat (LH), and specific humidity (Q)—are given in Figs. 14–16. Cumulative density function (CDF) plots of the mean pairwise differences (d03 or d04 vs d02) for each grid cell are shown by season in Fig. 17. The largest magnitude impact from WT arrays on Q is observed for both wind farm parameterizations in the summer months. Consistent with stronger near-surface warming in Fitch, grid cells with enhancement of Q exhibit slightly higher magnitudes in simulations with Fitch. Accordingly, in summer where air temperature at 2 m is warmer in Fitch, there is generally a small increase in Q downstream of WT (Fig. 16e). Spring is the season of maximum domainwide LH exchange (data from d02 without the action of WT; see Fig. 17c), while the SH flux is highest in summer (Fig. 17b). The perturbations in both LH and SH due to WT arrays, however, are of largest magnitude in summer for both schemes. Again, the perturbations are of slightly smaller magnitude in simulations with EWP. The median and mean perturbations from all grid cells in d03 and d04 for all seasons is $< |0.01| \text{ W m}^{-2}$. The samples of gridcell pairwise differences for all three parameters exhibit values that are symmetric around zero and all CDF curves cross zero at or very close to the 50th percentile, thus for both schemes the aggregated impact of WT arrays in Iowa has very little impact on the spatially averaged near-surface climate.

The mean gridcell differences between the domains with the WT parameterizations and the no-WT domain all indicate the effects on these thermodynamic variables are most pronounced during summer, with the spring months also showing some moderate impact. The latter is likely the result of feedback from the domainwide difference in 2-m temperature observed during those months. Even during summer, WT impact on SH and LH tends to be fairly modest compared to the domainwide mean energy fluxes (Fig. 17), although the upper and lowest one percent of grid cells exhibit perturbations in excess of 27 W m^{-2} . Figures 14e,f and 15e,f indicate that the differences are not localized to grid cells containing WT, or those adjacent cells, but are domainwide, and are not spatially coherent. For specific humidity (Fig. 16), the

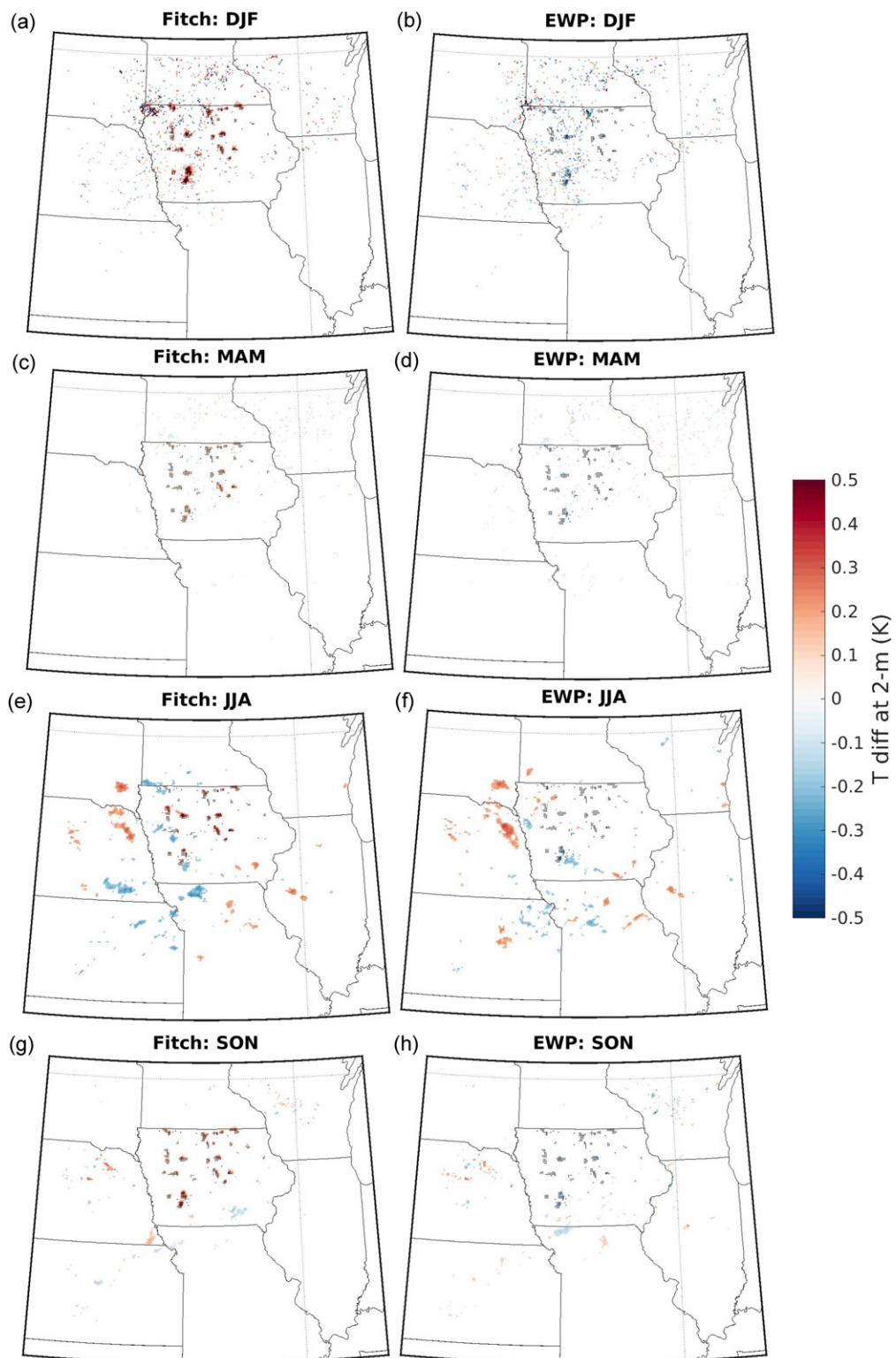


FIG. 12. Similar to Fig. 6, but for difference in air temperature at 2 m AGL for each grid cell within the inner domain (4 km). The difference is calculated for all simulated hourly values of air temperature over each season. The black dots represent grid cells that contain WT in Iowa.

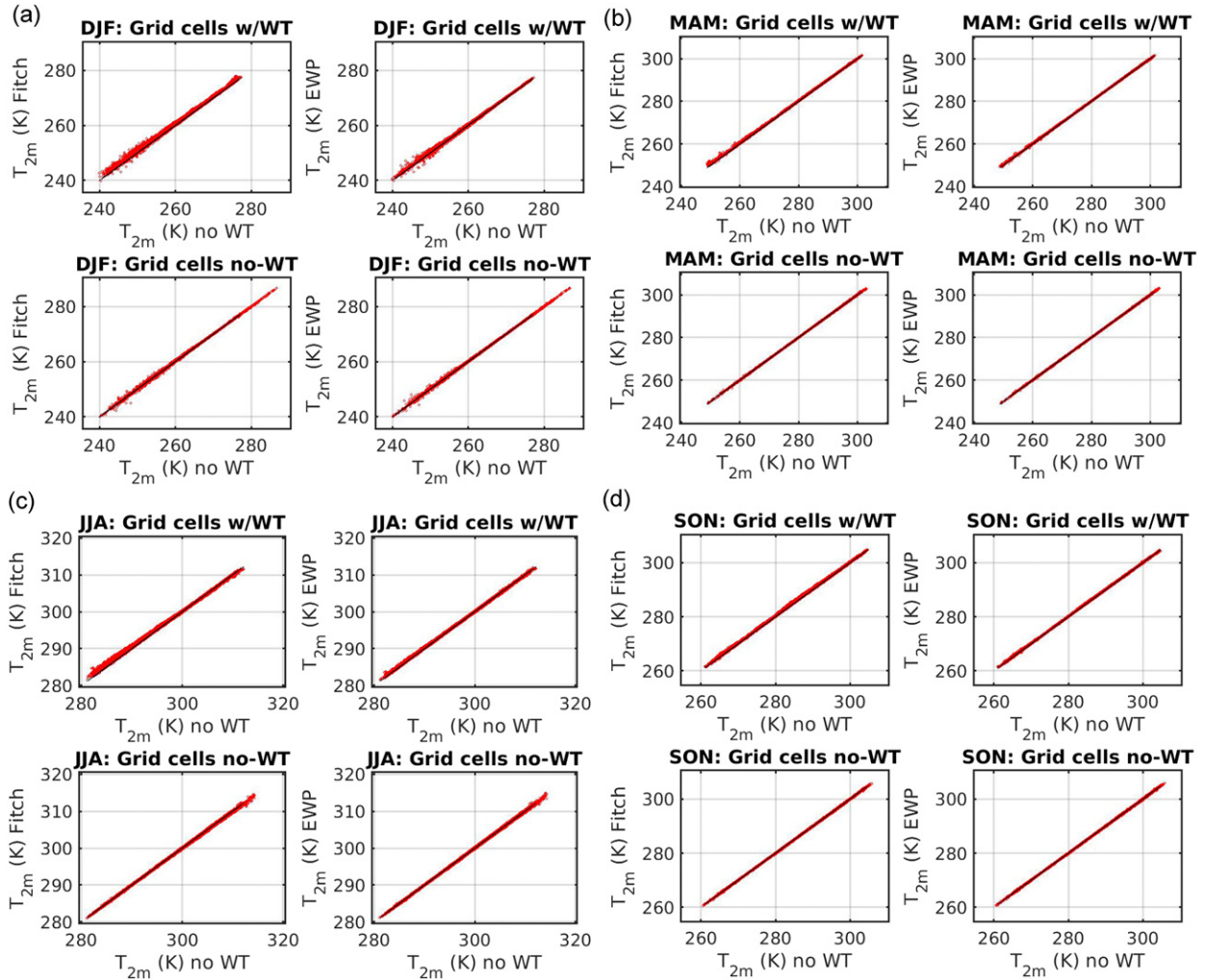


FIG. 13. Empirical quantile–quantile plots of the seasonal difference [(a) DJF, (b) MAM, (c) JJA, and (d) SON] in air temperature at 2 m AGL. For each four-plot group, the top two plots are for grid cells with WT and the bottom two plots for grid cells containing no WT, for Fitch (left two plots) and EWP (right two plots). Refer to Fig. 2 for the location of WT grid cells and the locations of the randomly selected background (no WT) grid cells.

differences between the two WT parameterizations are of largest magnitude in summer months (Fig. 17) with larger magnitude impacts (of up to 0.55 g kg^{-1}) from the Fitch wind farm parameterization. This maximum gridcell mean perturbation of Q represents a 5% difference on the domainwide average specific humidity at 2 m AGL.

The differences in near-surface climate impacts from WT arrays from the Fitch and EWP schemes are consistent with, and are the result of, three key differences in these wind farm parameterizations: 1) the relative speed-up in near-surface winds as simulated by Fitch, 2) differences in the mechanisms by which low-level TKE is modified and thus the feedback to PBL dynamics, and 3) the intensity of the vertical wind shear downstream of WT arrays.

4. Discussion and conclusions

The objective of this study was to provide a first assessment of the impacts of the two different wind farm parameterization schemes available for use with WRF in terms of the implications for 1) the magnitude, intensity, and downstream manifestations of wind farm wakes; 2) systemwide efficiency of power production from dense but irregularly spaced actual wind farm developments; and 3) local to regional climate effects from WT arrays. There are four major findings of this research:

- 1) Wind turbine array wakes are generally strongest in summer months, but winter also shows the presence of persistent velocity deficits downstream of major wind farm arrays.

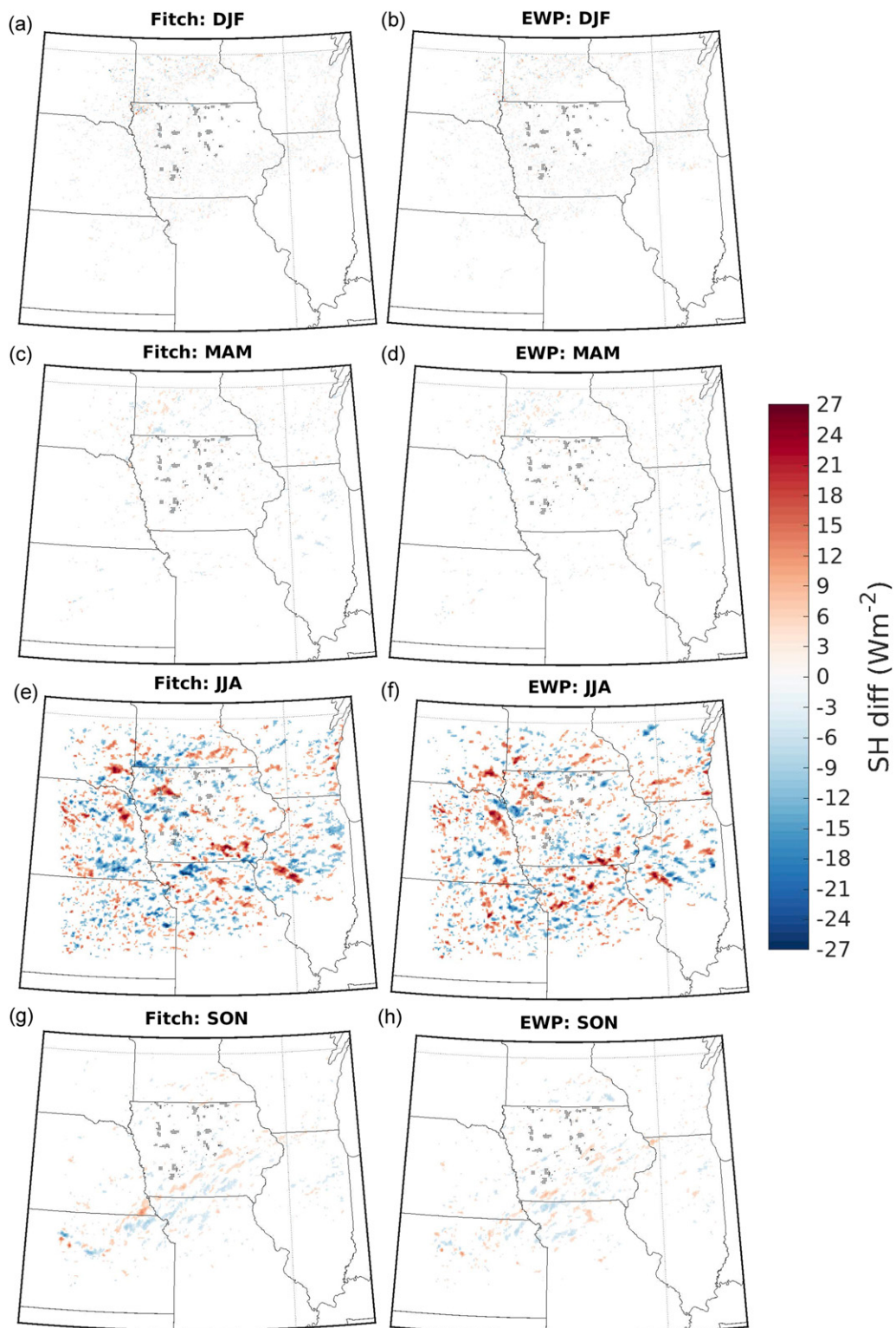


FIG. 14. As in Fig. 12, but for differences in sensible heat flux (SH), computed as the output from d03 or d04 minus d02; thus, positive values indicate higher SH in the domains in which the wind farm parameterizations are operating.

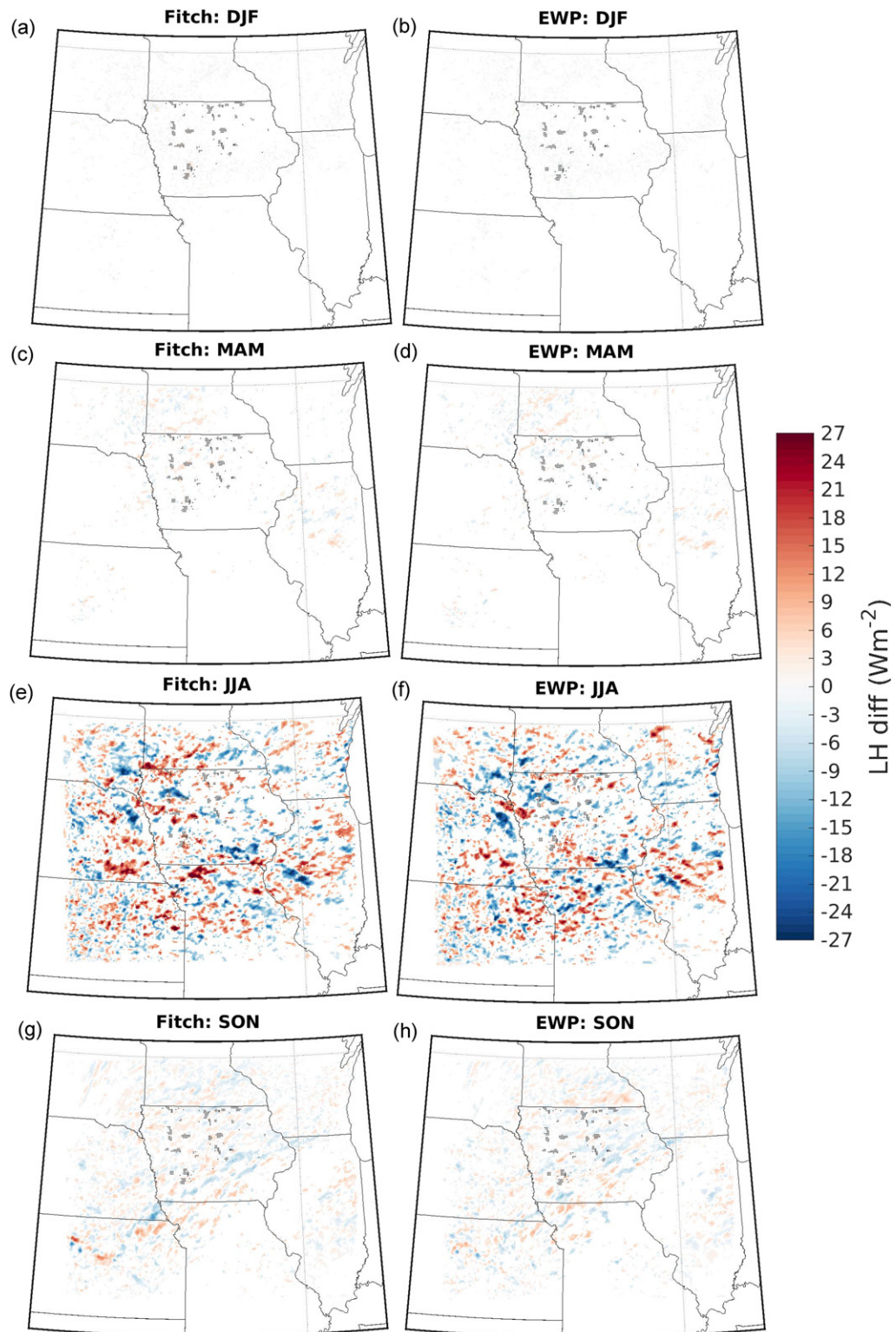


FIG. 15. As in Fig. 14, but for differences in latent heat flux (LH).

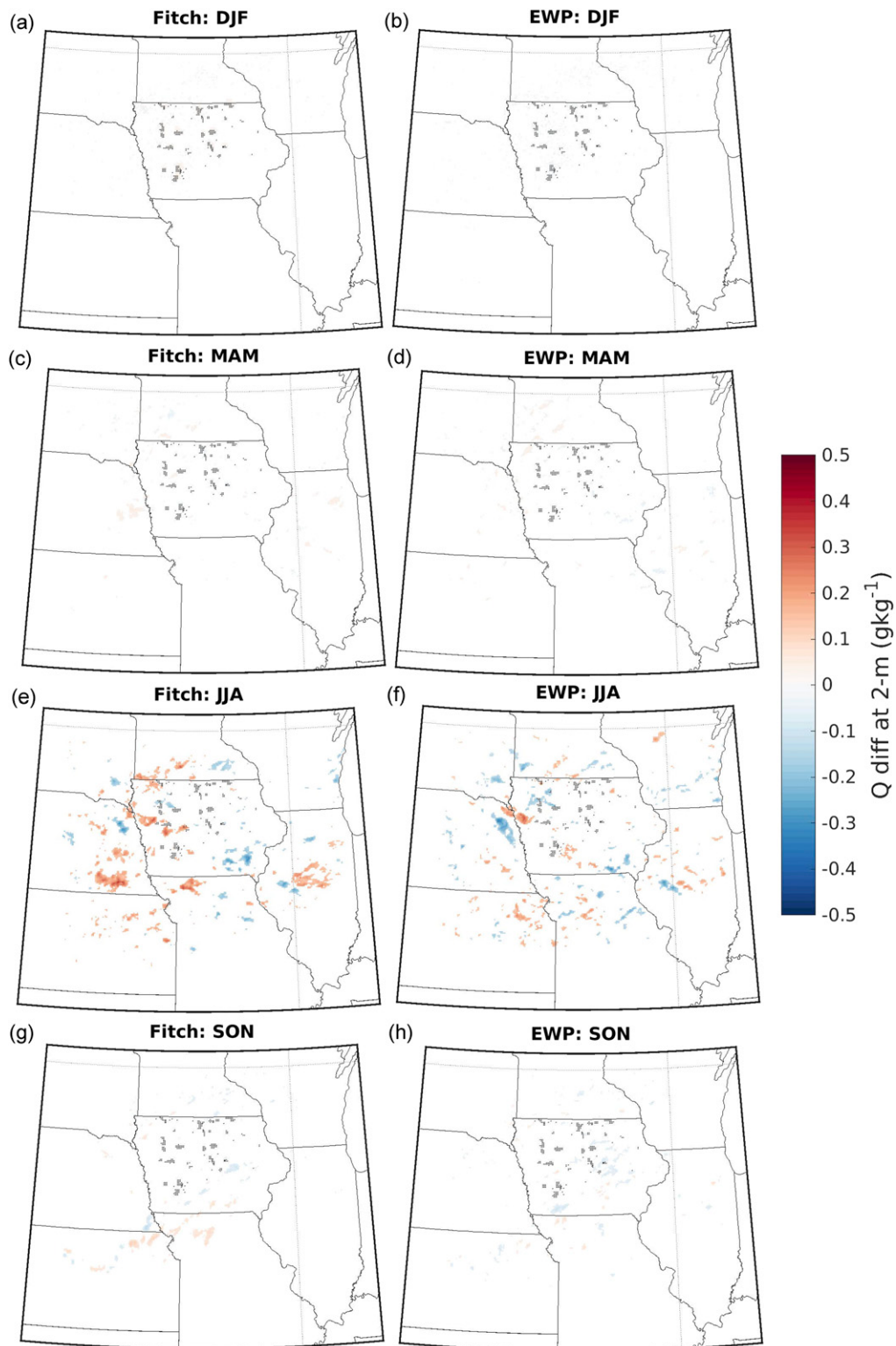


FIG. 16. As in Fig. 14, but for differences in specific humidity at 2 m. Positive values indicate higher near-surface specific humidity in the domains in which the wind farm parameterizations are operating.

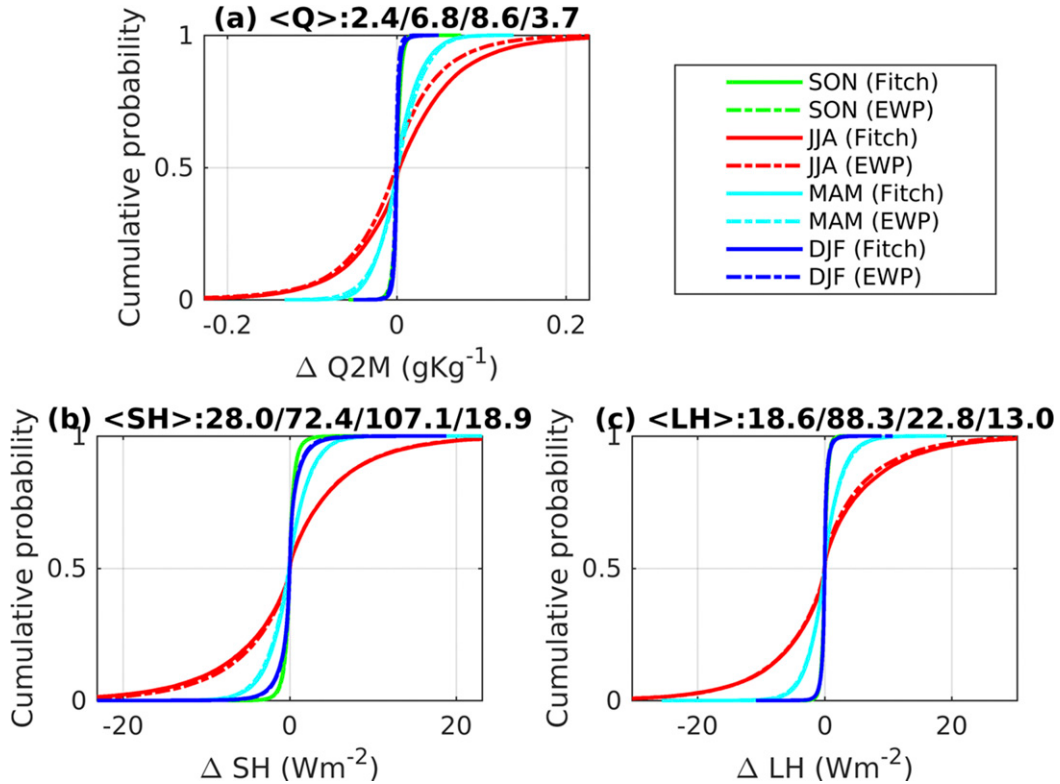


FIG. 17. Cumulative density function (From first to 99th percentile) of mean pairwise differences [d02 vs d03 (Fitch) or d04 (EWP)] for each grid cell in the inner domain of (a) specific humidity Q at 2 m AGL, (b) SH, and (c) LH in the inner domain (4 km). The labels at the topic of each frame show the domainwide seasonal mean value for each variable in output from domain 2 (DJF/MAM/JJA/SON) where no WT were operating.

- 2) The velocity deficits within and downstream of WT arrays are systematically of larger magnitude when the Fitch wind farm parameterization is used. Vertical and horizontal profiles of velocity deficits from a major cluster of wind farms show larger magnitude velocity deficits within the wind farms. For the WT cluster examined herein there is evidence for a faster downstream wake recovery to $< 5\%$ of the “freestream” wind speed when the EWP wind farm parameterization is used than when the Fitch scheme is applied.
- 3) The overall systemwide efficiency in terms of power production is shown to be 2%–3% higher when the EWP scheme is used. This is due to the smaller magnitude velocity deficits within major wind farm clusters and faster downstream wake recovery in this scheme.
- 4) Both wind farm parameterization schemes show climate impact from the operation of WT in Iowa, but these are of modest magnitude and generally confined to summer months. Consistent with the weaker wakes from WT arrays, the downstream effects on near-surface climate properties are also

more modest when the EWP scheme is used. Further, consistent with previous research using only the Fitch scheme (Pryor et al. 2018a), even for the relatively high WT installed capacity densities in Iowa, have little impact beyond the grid cells in which WT are deployed and the lack spatial coherence that would imply substantial impact on regional climate.

This study thus illustrates the sensitivity arising from the choice of wind farm parameterization used. It is thus a contribution to a topic that has not been explored to any great detail in the literature and is an extension of work presented in Fitch et al. (2013) that compared use of an explicit wind farm parameterization with use of enhanced roughness blocks. The key sensitivities arising from the operation of each wind farm parameterization are compared and summarized in a flow diagram (Fig. 18). In the absence of field validation experiments, it is not possible to assert which wind farm parameterization is optimal for use on land or what length scale should be applied in the EWP scheme for a specific modeling context. It is worthy of note that the differences in the wind farm parameterizations in terms of

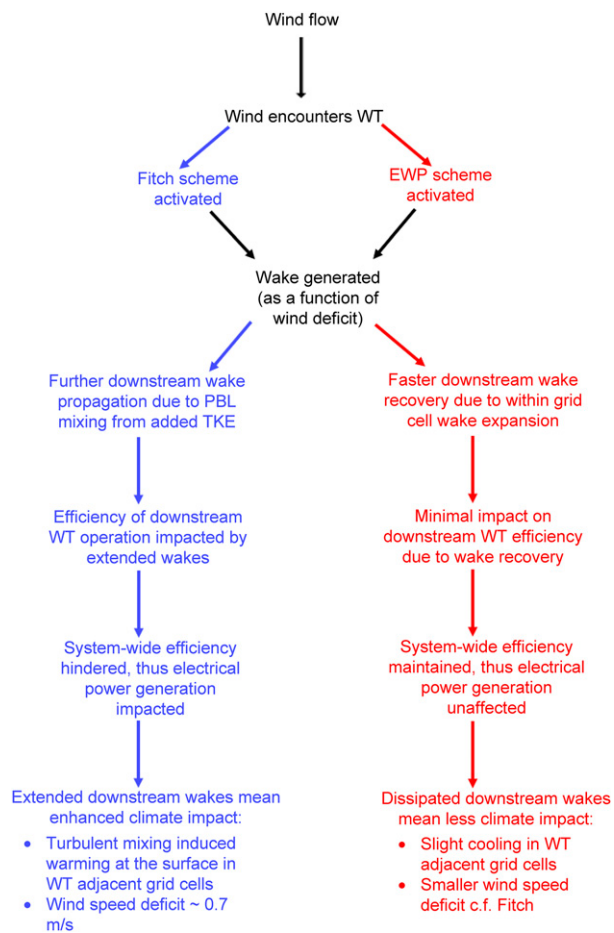


FIG. 18. Flow diagram summarizing the key simulation differences arising from the operation of the Fitch (blue) and EWP (red) WT parameterization schemes.

wake intensity are most marked within and near to WT arrays and that at greater downstream distances the schemes produce relatively similar results in terms of the vertical profiles and magnitudes of the velocity deficits. There are a number of reasons why this is the case, the within-gridcell diffusion of the wakes in the EWP scheme plays a major role in dictating the initial magnitude of the velocity deficits, while the addition of TKE in the Fitch scheme has a more profound impact on the downstream recovery.

It is important to reiterate that it is not currently possible to differentiate the relative skill (or fidelity) of the two wind farm parameterizations. Thus, no recommendation can be made about when or where either scheme is more appropriate. However, this work does illustrate the need for large-scale field experiments to be conducted in a range of climate/environmental settings for a range of wind turbine deployment strategies. The importance of differences in wake magnitudes from the

two wind farm schemes can be demonstrated as follows: Using a conservative estimate of price paid by MW h of \$25, if realized, an additional 1 TW h of annual electricity production from WT in Iowa would equate to an annual revenue of \$25 million. Further, the short downwind distances for wake recovery to 5% of the freestream indicated by use of the EWP scheme might make some sites in the shadow of existing wind farm arrays viable for development.

There are some important caveats to our findings. We selected to run the simulation as a continuous integration (as is commonly done within the atmospheric science community) without reinitialization every few days (as proposed by Lo et al. 2008) to reduce model drift. This may have negatively impacted the fidelity of the simulations relative to reanalysis output but should have minimal impact on the comparison of the two wind farm parameterizations. Model evaluation against ERA5 reanalysis data indicates that wind speeds from WRF are positively biased against this reanalysis product, but exhibit similar spatial patterns, as expected a priori due to the use of reanalysis lateral boundary conditions. The positive bias in wind speeds within the WT rotor plane leads to a positive bias in gross CF, particularly in the summer months. It is important to recall that the wind farm schemes applied herein are not designed to describe wakes from individual WT but rather the cumulative impact from multiple WT on the flow field. Use of a 4-km grid resolution is intended to reduce the number of WT in individual grid cells relative to most previous research and thus reduce the error introduced by assuming all WT within a specific grid cell experience the same inflow wind profile. Nevertheless, the computational and storage demands for these high-resolution, regional-scale simulations for a whole year are considerable and there may be limited benefits to finer horizontal and vertical resolution. The length scale used within EWP requires tuning based on the particular WT type. While a large majority of WT in Iowa have similar characteristics to the WT used in Volker et al. (2015) (including the Pomeroy WT used for wake analyses), it is possible that some of the differences between the Fitch and EWP schemes presented herein could be reconciled by use of a different length scale. In the absence of wake data to quantify this length scale and the actual observed wakes for Iowa WT, it would be premature to make recommendations with regard to which wind farm parameterization exhibits superior fidelity. Future research should focus on detailed analyses of other areas with major wind farm developments in order to evaluate the importance of regional climate to differences in the wind farm parameterizations, include analyses of the resolution dependence of the two schemes,

and include longer duration simulations to examine the degree to which our findings are robust to interannual variability in wind climates (Pryor et al. 2018b).

Acknowledgments. The U.S. Department of Energy (DOE) (DE-SC0016438) and Cornell University's Atkinson Center for a Sustainable Future (ACSF-sp2279-2016) funded this research. We thank Adam Brazier, Brandon Barker, and Bennett Wineholt for their assistance in building and maintaining the cloud infrastructure leveraged in this research. We gratefully acknowledge Patrick Volker of the Technical University of Denmark for supplying the EWP code and both him and Andrea Hahmann for very useful discussions. This research was enabled by access to a range of computational resources supported by NSF ACI-1541215, those made available via the NSF Extreme Science and Engineering Discovery Environment (XSEDE) (Award TG-ATM170024), and those of the National Energy Research Scientific Computing Center, which is a DOE Office of Science User Facility supported by the Office of Science under Contract DE-AC02-05CH11231. Comments from three reviewers are gratefully acknowledged.

Data availability statement: ERA-Interim output is available online (<http://apps.ecmwf.int/datasets/>). The WT locations as reported by the USGS are available online (<https://eerscmap.usgs.gov/arcgis/rest/services/wind/wTurbinesWMDyn/MapServer>). The NOAA/NCEP real-time global sea surface temperature analyses are available online (<http://www.nco.ncep.noaa.gov/pmb/products/sst>). ERA5 output is available online (<https://cds.climate.copernicus.eu/cdsapp#!/home>). The EWP scheme is available by request from Patrick Volker (pvol@dtu.dk). The WRF Model output generated within this project (including the namelist used) is available online (http://portal.nersc.gov/archive/home/projects/m2645/www/public_data_fitch_EWP).

REFERENCES

- AWEA, 2014: 2014 U.S. wind industry annual market report. Accessed 27 February 2019, <https://www.awea.org/resources/publications-and-reports/market-reports/2014-u-s-wind-industry-market-reports>.
- , 2015: 2015 U.S. wind industry annual market report. Accessed 27 February 2019, <https://www.awea.org/resources/publications-and-reports/market-reports/2015-u-s-wind-industry-market-reports>.
- , 2016: 2016 U.S. wind industry annual market report. Accessed 27 February 2019, <https://www.awea.org/resources/publications-and-reports/market-reports/2016-u-s-wind-industry-market-reports>.
- AWS Truepower LLC, 2010: Iowa 80-meter wind resource map. Accessed 27 February 2019, <https://windexchange.energy.gov/maps-data/32>.
- Baidya Roy, S., 2011: Simulating impacts of wind farms on local hydrometeorology. *J. Wind Eng. Ind. Aerodyn.*, **99**, 491–498, <https://doi.org/10.1016/j.jweia.2010.12.013>.
- , and J. J. Traiteur, 2010: Impacts of wind farms on surface air temperature. *Proc. Natl. Acad. Sci. USA*, **107**, 17899–17904, <https://doi.org/10.1073/pnas.1000493107>.
- , S. W. Pacala, and R. Walko, 2004: Can large wind farms affect local meteorology? *J. Geophys. Res.*, **109**, D19101, <https://doi.org/10.1029/2004JD004763>.
- Barrie, D. B., and D. B. Kirk-Davidoff, 2010: Weather response to a large wind turbine array. *Atmos. Chem. Phys.*, **10**, 769–775, <https://doi.org/10.5194/acp-10-769-2010>.
- Barthelmie, R. J., and S. C. Pryor, 2013: An overview of data for wake model evaluation in the Virtual Wakes Laboratory. *Appl. Energy*, **104**, 834–844, <https://doi.org/10.1016/j.apenergy.2012.12.013>.
- , K. S. Hansen, and S. C. Pryor, 2013: Meteorological controls on wind turbine wakes. *Proc. IEEE*, **101**, 1010–1019, <https://doi.org/10.1109/JPROC.2012.2204029>.
- Carroll, J., A. McDonald, I. Dinwoodie, D. McMillan, M. Revie, and I. Lazakis, 2017: Availability, operation and maintenance costs of offshore wind turbines with different drive train configurations. *Wind Energy*, **20**, 361–378, <https://doi.org/10.1002/we.2011>.
- Cervarich, M. C., S. B. Roy, and L. Zhou, 2013: Spatiotemporal structure of wind farm-atmospheric boundary layer interactions. *Energy Procedia*, **40**, 530–536, <https://doi.org/10.1016/j.egypro.2013.08.061>.
- Chen, F., and J. Dudhia, 2001: Coupling an advanced land surface-hydrology model with the Penn State–NCAR MM5 modeling system. Part I: Model implementation and sensitivity. *Mon. Wea. Rev.*, **129**, 569–585, [https://doi.org/10.1175/1520-0493\(2001\)129<0569:CAALSH>2.0.CO;2](https://doi.org/10.1175/1520-0493(2001)129<0569:CAALSH>2.0.CO;2).
- Copernicus Climate Change Service, 2017: ERA5 monthly averaged data on single levels from 1979 to present. ECMWF, accessed 27 February 2019, <https://doi.org/10.24381/cds.f17050d7>.
- Dee, D. P., and Coauthors, 2011: The ERA-Interim reanalysis: Configuration and performance of the data assimilation system. *Quart. J. Roy. Meteor. Soc.*, **137**, 553–597, <https://doi.org/10.1002/qj.828>.
- Diffendorfer, J. E., R. W. Compton, L. A. Kramer, Z. H. Ancona, and D. Norton, 2015a: Onshore industrial wind turbine locations for the United States to March 2014: U.S. Geological Survey data release. USGS, accessed 23 March 2017, <https://doi.org/10.5066/F7251G8Q>.
- , L. A. Kramer, Z. H. Ancona, and C. P. Garrity, 2015b: Onshore industrial wind turbine locations for the United States up to March 2014. *Sci. Data*, **2**, 150060, <https://doi.org/10.1038/sdata.2015.60>.
- Draxl, C., A. N. Hahmann, A. Peña, and G. Giebel, 2014: Evaluating winds and vertical wind shear from Weather Research and Forecasting model forecasts using seven planetary boundary layer schemes. *Wind Energy*, **17**, 39–55, <https://doi.org/10.1002/we.1555>.
- Dudhia, J., 1989: Numerical study of convection observed during the winter monsoon experiment using a mesoscale two-dimensional model. *J. Atmos. Sci.*, **46**, 3077–3107, [https://doi.org/10.1175/1520-0469\(1989\)046<3077:NSOCOD>2.0.CO;2](https://doi.org/10.1175/1520-0469(1989)046<3077:NSOCOD>2.0.CO;2).
- Ek, M., and Coauthors, 2003: Implementation of Noah land surface model advances in the National Centers for Environmental Prediction operational mesoscale Eta model. *J. Geophys. Res.*, **108**, 8851, <https://doi.org/10.1029/2002JD003296>.
- Fiedler, B., and M. Bukovsky, 2011: The effect of a giant wind farm on precipitation in a regional climate model. *Environ. Res. Lett.*, **6**, 045101, <https://doi.org/10.1088/1748-9326/6/4/045101>.

- Fitch, A. C., 2016: Notes on using the mesoscale wind farm parameterization of Fitch et al. (2012) in WRF. *Wind Energy*, **19**, 1757–1758, <https://doi.org/10.1002/we.1945>.
- , J. B. Olson, J. K. Lundquist, J. Dudhia, A. K. Gupta, J. Michalakes, and I. Barstad, 2012: Local and mesoscale impacts of wind farms as parameterized in a mesoscale NWP model. *Mon. Wea. Rev.*, **140**, 3017–3038, <https://doi.org/10.1175/MWR-D-11-00352.1>.
- , —, and —, 2013: Parameterization of wind farms in climate models. *J. Climate*, **26**, 6439–6458, <https://doi.org/10.1175/JCLI-D-12-00376.1>.
- Gao, Y., J. S. Fu, J. B. Drake, Y. Liu, and J.-F. Lamarque, 2012: Projected changes of extreme weather events in the eastern United States based on a high resolution climate modeling system. *Environ. Res. Lett.*, **7**, 044025, <https://doi.org/10.1088/1748-9326/7/4/044025>.
- Hacker, J. P., J. Exby, D. Gill, I. Jimenez, C. Maltzahn, T. See, G. Mullendore, and K. Fossell, 2017: A containerized mesoscale model and analysis toolkit to accelerate classroom learning, collaborative research, and uncertainty quantification. *Bull. Amer. Meteor. Soc.*, **98**, 1129–1138, <https://doi.org/10.1175/BAMS-D-15-00255.1>.
- Hahmann, A. N., C. L. Vincent, A. Peña, J. Lange, and C. B. Hasager, 2015: Wind climate estimation using WRF model output: Method and model sensitivities over the sea. *Int. J. Climatol.*, **35**, 3422–3439, <https://doi.org/10.1002/joc.4217>.
- Harris, R. A., L. Zhou, and G. Xia, 2014: Satellite observations of wind farm impacts on nocturnal land surface temperature in Iowa. *Remote Sens.*, **6**, 12 234–12 246, <https://doi.org/10.3390/rs61212234>.
- Hersbach, H., and D. Dee, 2016: ERA5 reanalysis is in production. *ECMWF Newsletter*, No. 147, ECMWF, Reading, United Kingdom, 7, <http://www.ecmwf.int/sites/default/files/elibrary/2016/16299-newsletter-no147-spring-2016.pdf>.
- Hoffmann, L., and Coauthors, 2019: From ERA-Interim to ERA5: The considerable impact of ECMWF's next-generation reanalysis on Lagrangian transport simulations. *Atmos. Chem. Phys.*, **19**, 3097–3124, <https://doi.org/10.5194/acp-19-3097-2019>.
- Jiménez, P. A., J. Dudhia, J. F. González-Rouco, J. Navarro, J. P. Montávez, and E. García-Bustamante, 2012: A revised scheme for the WRF surface layer formulation. *Mon. Wea. Rev.*, **140**, 898–918, <https://doi.org/10.1175/MWR-D-11-00056.1>.
- Kain, J. S., and J. M. Fritsch, 1993: Convective parameterization for mesoscale models: The Kain-Fritsch scheme. *The Representation of Cumulus Convection in Numerical Models*, Meteor. Monogr., No. 46, Amer. Meteor. Soc., 165–170.
- Kalverla, P. C., J. B. Duncan Jr., G. J. Steeneveld, and A. A. M. Holtslag, 2019: Low-level jets over the North Sea based on ERA5 and observations: Together they do better. *Wind Energy Sci.*, **4**, 193–209, <https://doi.org/10.5194/wes-4-193-2019>.
- Keith, D., J. DeCarolis, D. Denkenberger, D. Lenschow, S. Malyshev, S. Pacala, and P. Rasch, 2004: The influence of large-scale wind power on global climate. *Proc. Natl. Acad. Sci. USA*, **101**, 16 115–16 120, <https://doi.org/10.1073/pnas.0406930101>.
- Lee, J. C. Y., and J. K. Lundquist, 2017: Evaluation of the wind farm parameterization in the Weather Research and Forecasting model (version 3.8.1) with meteorological and turbine power data. *Geosci. Model Dev.*, **10**, 4229–4244, <https://doi.org/10.5194/gmd-10-4229-2017>.
- Lo, J. C.-F., Z.-L. Yang, and R. A. Pielke Sr., 2008: Assessment of three dynamical climate downscaling methods using the Weather Research and Forecasting (WRF) model. *J. Geophys. Res.*, **113**, D09112, <https://doi.org/10.1029/2007JD009216>.
- Mearns, L. O., and Coauthors, 2012: The North American Regional Climate Change Assessment Program: Overview of phase I results. *Bull. Amer. Meteor. Soc.*, **93**, 1337–1362, <https://doi.org/10.1175/BAMS-D-11-00223.1>.
- Miller, L. M., N. A. Brunsell, D. B. Mechem, F. Gans, A. J. Monaghan, R. Vautard, D. W. Keith, and A. Kleidon, 2015: Two methods for estimating limits to large-scale wind power generation. *Proc. Natl. Acad. Sci. USA*, **112**, 11 169–11 174, <https://doi.org/10.1073/pnas.1408251112>.
- Mlawer, E. J., S. J. Taubman, P. D. Brown, M. J. Iacono, and S. A. Clough, 1997: Radiative transfer for inhomogeneous atmospheres: RRTM, a validated correlated-k model for the longwave. *J. Geophys. Res.*, **102**, 16 663–16 682, <https://doi.org/10.1029/97JD00237>.
- Nakanishi, M., and H. Niino, 2006: An improved Mellor–Yamada level-3 model: Its numerical stability and application to a regional prediction of advection fog. *Bound.-Layer Meteor.*, **119**, 397–407, <https://doi.org/10.1007/s10546-005-9030-8>.
- National Renewable Energy Laboratory, 2008: 20% wind energy by 2030: Increasing wind energy's contribution to US electricity supply. U.S. Department of Energy Rep. DOE/GO-102008-2567, 248 pp., <http://www.nrel.gov/docs/fy08osti/41869.pdf>.
- , 2015: Wind Vision: A new era for wind power in the United States. U.S. Department of Energy Rep. DOE/GO-102015-4557, 348 pp., http://www.energy.gov/sites/prod/files/WindVision_Report_final.pdf.
- Olauson, J., 2018: ERA5: The new champion of wind power modelling? *Renewable Energy*, **126**, 322–331, <https://doi.org/10.1016/j.renene.2018.03.056>.
- Piles, M., J. Ballabriga-Poy, and J. Muñoz-Sabater, 2019: Dominant features of global surface soil moisture variability observed by the SMOS satellite. *Remote Sens.*, **11**, 95, <https://doi.org/10.3390/rs11010095>.
- Pryor, S. C., and A. N. Hahmann, 2019: Downscaling wind. *Oxford Research Encyclopedia on Climate Science*, H. von Storch, Ed., Oxford University Press, <https://doi.org/10.1093/acrefore/9780190228620.013.730>.
- , M. Nielsen, R. J. Barthelmie, and J. Mann, 2004: Can satellite sampling of offshore wind speeds realistically represent wind speed distributions? Part II: Quantifying uncertainties associated with distribution fitting methods. *J. Appl. Meteor.*, **43**, 739–750, <https://doi.org/10.1175/2096.1>.
- , R. J. Barthelmie, and T. Shepherd, 2018a: The influence of real-world wind turbine deployments on local to mesoscale climate. *J. Geophys. Res.*, **123**, 5804–5826, <https://doi.org/10.1029/2017JD028114>.
- , T. J. Shepherd, and R. J. Barthelmie, 2018b: Interannual variability of wind climates and wind turbine annual energy production. *Wind Energy Sci.*, **3**, 651–665, <https://doi.org/10.5194/wes-3-651-2018>.
- , R. J. Barthelmie, A. Hahmann, T. J. Shepherd, and P. J. H. Volker, 2018c: Downstream effects from contemporary wind turbine deployments. *J. Phys. Conf. Ser.*, **1037**, 072010, <https://doi.org/10.1088/1742-6596/1037/7/072010>.
- , T. J. Shepherd, M. Bukovsky, and R. J. Barthelmie, 2020: Assessing the stability of wind resource and operating conditions. *J. Phys. Conf. Ser.*, in press.
- Rajewski, D. A., and Coauthors, 2013: Crop Wind Energy Experiment (CWEX): Observations of surface-layer, boundary layer, and mesoscale interactions with a wind farm. *Bull. Amer. Meteor. Soc.*, **94**, 655–672, <https://doi.org/10.1175/BAMS-D-11-00240.1>.
- Reynolds, R. W., and D. B. Chelton, 2010: Comparisons of daily sea surface temperature analyses for 2007–08. *J. Climate*, **23**, 3545–3562, <https://doi.org/10.1175/2010JCLI3294.1>.

- Rogers, E., T. Black, B. Ferrier, Y. Lin, D. Parrish, and G. DiMego, 2001: Changes to the NCEP Meso Eta analysis and forecast system: Increase in resolution, new cloud microphysics, modified precipitation assimilation, modified 3DVAR analysis. NWS Tech. Procedures Bull., 15 pp.
- Skamarock, W. C., and Coauthors, 2008: A description of the Advanced Research WRF version 3. NCAR Tech. Note NCAR/TN-475+STR, 113 pp., [http://doi.org/10.5065/D68S4MVH](https://doi.org/10.5065/D68S4MVH).
- Smith, C. M., R. J. Barthelmie, and S. C. Pryor, 2013: In situ observations of the influence of a large onshore wind farm on near-surface temperature, turbulence intensity and wind speed profiles. *Environ. Res. Lett.*, **8**, 034006, <https://doi.org/10.1088/1748-9326/8/3/034006>.
- Staid, A., C. VerHulst, and S. D. Guikema, 2018: A comparison of methods for assessing power output in non-uniform onshore wind farms. *Wind Energy*, **21**, 42–52, <https://doi.org/10.1002/we.2143>.
- Sun, X., M. Xue, J. Brotzge, R. A. McPherson, X.-M. Hu, and X.-Q. Yang, 2016: An evaluation of dynamical downscaling of Central Plains summer precipitation using a WRF-based regional climate model at a convection-permitting 4 km resolution. *J. Geophys. Res. Atmos.*, **121**, 13 801–13 825, <https://doi.org/10.1002/2016JD024796>.
- Taylor, K. E., 2001: Summarizing multiple aspects of model performance in a single diagram. *J. Geophys. Res.*, **106**, 7183–7192, <https://doi.org/10.1029/2000JD900719>.
- U.S. Energy Information Administration, 2000: Form EIA-923 detailed electric power data. Subsets used: 2014, 2015, 2016, EIA, accessed 27 February 2019, <https://www.eia.gov/electricity/data/eria923/>.
- , 2015: Electric power monthly, with data for December 2014. EIA Rep., 227 pp., <https://www.eia.gov/electricity/monthly/archive/february2015.pdf>.
- Vautard, R., F. Thais, I. Tobin, F.-M. Bréon, J.-G. D. de Lavergne, A. Colette, P. You, and P. M. Ruti, 2014: Regional climate model simulations indicate limited climatic impacts by operational and planned European wind farms. *Nat. Commun.*, **5**, 3196, <https://doi.org/10.1038/ncomms4196>.
- Volker, P. J. H., J. Badger, A. N. Hahmann, and S. Ott, 2015: The Explicit Wake Parametrisation V1.0: A wind farm parametrisation in the mesoscale model WRF. *Geosci. Model Dev.*, **8**, 3715–3731, <https://doi.org/10.5194/gmd-8-3715-2015>.
- Wang, C., and R. G. Prinn, 2010: Potential climatic impacts and reliability of very large-scale wind farms. *Atmos. Chem. Phys.*, **10**, 2053–2061, <https://doi.org/10.5194/acp-10-2053-2010>.
- Wang, J., and V. R. Kotamarthi, 2014: Downscaling with a nested regional climate model in near-surface fields over the contiguous United States. *J. Geophys. Res. Atmos.*, **119**, 8778–8797, <https://doi.org/10.1002/2014JD021696>.
- Wang, Q., K. Luo, R. Yuan, S. Zhang, and J. Fan, 2019: Wake and performance interference between adjacent wind farms: Case study of Xinjiang in China by means of mesoscale simulations. *Energy*, **166**, 1168–1180, <https://doi.org/10.1016/j.energy.2018.10.111>.
- Wilks, D., 2011: *Statistical Methods in the Atmospheric Sciences*. 3rd ed. International Geophysics Series, Vol. 100, Academic Press, 676 pp.
- Wu, Y.-T., and F. Porté-Agel, 2013: Simulation of turbulent flow inside and above wind farms: Model validation and layout effects. *Bound.-Layer Meteor.*, **146**, 181–205, <https://doi.org/10.1007/s10546-012-9757-y>.
- Xia, G., M. Charles Cervarich, S. Baidya Roy, L. Zhou, J. Minder, P. Jimenez, and J. Freedman, 2017: Simulating impacts of real-world wind farms on land surface temperature using the WRF model: Validation with observations. *Mon. Wea. Rev.*, **145**, 4813–4836, <https://doi.org/10.1175/MWR-D-16-0401.1>.
- , L. Zhou, J. R. Minder, R. G. Fovell, and P. A. Jimenez, 2019: Simulating impacts of real-world wind farms on land surface temperature using the WRF model: Physical mechanisms. *Climate Dyn.*, **53**, 1723–1739, <https://doi.org/10.1007/s00382-019-04725-0>.
- Zhou, L., Y. Tian, S. Baidya Roy, C. Thorncroft, L. F. Bosart, and Y. Hu, 2012: Impacts of wind farms on land surface temperature. *Nat. Climate Change*, **2**, 539–543, <https://doi.org/10.1038/nclimate1505>.